

THE RADIO EMISSION, X-RAY EMISSION, AND HYDRODYNAMICS OF G328.4+0.2: A COMPREHENSIVE ANALYSIS OF A LUMINOUS PULSAR WIND NEBULA, ITS NEUTRON STAR, AND THE PROGENITOR SUPERNOVA EXPLOSION

JOSEPH D. GELFAND, PATRICK O. SLANE, AND DANIEL J. PATNAUDE
 Harvard-Smithsonian Center for Astrophysics, Cambridge, MA 02138

AND

B. M. GAENSLER*
 Harvard-Smithsonian Center for Astrophysics, Cambridge, MA 02138 and
 School of Physics, The University of Sydney, NSW 2006, Australia

JOHN P. HUGHES
 Department of Physics and Astronomy, Rutgers University, Piscataway, NJ 08854-8019

FERNANDO CAMILO
 Columbia Astrophysics Lab, Columbia University, New York, NY 10027
Draft version February 1, 2008

ABSTRACT

We present new observational results obtained for the Galactic non-thermal radio source G328.4+0.2 to determine both if this source is a pulsar wind nebula or supernova remnant, and in either case, the physical properties of this source. Using X-ray data obtained by *XMM*, we confirm that the X-ray emission from this source is heavily absorbed and has a spectrum best fit by a power law model of photon index $\Gamma = 2$ with no evidence for a thermal component, the X-ray emission from G328.4+0.2 comes from a region significantly smaller than the radio emission, and that the X-ray and radio emission are significantly offset from each other. We also present the results of a new high resolution ($7''$) 1.4 GHz image of G328.4+0.2 obtained using the Australia Telescope Compact Array, and a deep search for radio pulsations using the Parkes Radio Telescope. By comparing this 1.4 GHz image with a similar resolution image at 4.8 GHz, we find that the radio emission has a flat spectrum ($\alpha \approx 0$; $S_\nu \propto \nu^\alpha$), though some areas of the eastern edge of G328.4+0.2 have a steeper radio spectral index of $\alpha \sim -0.3$. Additionally, we searched without success for a central radio pulsar, and obtain a luminosity limit of $L_{1400} < \lesssim 30 \text{ mJy kpc}^2$, assuming a distance of 17 kpc. In light of these observational results, we test if G328.4+0.2 is a pulsar wind nebula (PWN) or a large PWN inside a supernova remnant (SNR) using a simple hydrodynamic model for the evolution of a PWN inside a SNR. As a result of this analysis, we conclude that G328.4+0.2 is a young ($\lesssim 10000$ years old) pulsar wind nebula formed by a low magnetic field ($\lesssim 10^{12}$ G) neutron star born spinning rapidly ($\lesssim 10$ ms) expanding into an undetected SNR formed by an energetic ($\gtrsim 10^{51}$ ergs), low ejecta mass ($M_{\text{ej}} \lesssim 5 M_\odot$) supernova explosion which occurred in a low density ($n \sim 0.03 \text{ cm}^{-3}$) environment. If correct, the low magnetic field and fast initial spin period of this neutron star poses problems for models of magnetar formation which require fast initial periods.

Subject headings: stars: neutron, stars: pulsars: general, ISM: supernova remnants, radio continuum: ISM, X-rays: individual

1. INTRODUCTION

Stars with initial masses between ~ 9 and $25 M_\odot$ are expected to end their lives in a giant supernova (SN) explosion during which neutron stars are created. The fast moving ejecta from the SN create a supernova remnant (SNR), while the particle wind produced by the neutron star as it loses rotational energy inflates a pulsar wind nebula (PWN; Gaensler & Slane 2006). Initially, the PWN is inside the SNR – and when the PWN is detected inside the SNR the system is called a “composite” SNR (Helfand & Becker 1987). The evolution of the central neutron star and the outer SNR affect the PWN,

and as a result the PWN goes through several evolutionary phases while it is inside the SNR. This evolution is determined by the physical properties of the neutron star (specifically the initial period P_0 , the braking index p^1 , and the strength of the dipole component to the surface magnetic field B_{ns}), the SN explosion (explosion energy E_{sn} and ejecta mass M_{ej}), and the surrounding medium (ambient number density n). As a result, by measuring the properties of the PWN inside a SNR at a given time one is able to constrain these physical parameters which allows one to study the mechanisms behind both core-collapse SNe and massive star evolution.

With this in mind, we present results of new radio

Electronic address: jgelfand@cfa.harvard.edu

*Alfred P. Sloan Research Fellow, Australian Research Council Federation Fellow

Electronic address: jgelfand@cfa.harvard.edu

¹ The braking index is defined as $\dot{\Omega} \propto \Omega^p$, where Ω is the angular velocity of the neutron star’s surface.

observations of this source with the Australia Telescope Compact Array (ATCA), as well as a new X-ray (X-ray Multi-mirror Mission; *XMM*) observation of G328.4+0.2 (MSH 15-57; Mills et al. 1961). This source is a distant ($d \geq 17.4 \pm 0.9$ kpc; Gaensler et al. 2000), radio bright (flux density $S_\nu = 14.3 \pm 0.1$ Jy at $\nu = 1.4$ GHz), polarized, extended (diameter $D \simeq 5.0'$) radio source with a relatively flat spectral index ($\alpha \simeq -0.12 \pm 0.03$ where $S_\nu \propto \nu^\alpha$; Gaensler et al. 2000). Based on these radio properties, and the discovery of non-thermal X-ray emission from this source by *ASCA* (Hughes et al. 2000), this source was classified as a PWN – the largest and most radio-luminous PWN in the Galaxy. In this interpretation, the expectation is that G328.4+0.2 is ~ 7000 years old and powered by an extremely energetic neutron star (Gaensler et al. 2000). However, follow up radio polarimetry work (Johnston et al. 2004) implied that G328.4+0.2 is an older composite SNR in which the PWN is just a small fraction of the total volume, and as a result is powered by a significantly less energetic neutron star then argued by Gaensler et al. (2000). In this paper, we analyze new observations of this source in order to determine the age of G328.4+0.2, the energetics of the neutron star and the progenitor SN, and the density of its environment.

In §2 we present new X-ray and radio observations of G328.4+0.2. In §3, we first discuss the expected evolutionary sequence for PWNs inside SNRs (§3.1), making general comments regarding the expected observational signature of each phase. In §3.2 we use the observational results presented in §2 to draw some initial conclusions about the nature of G328.4+0.2. In §4, we present a simple hydrodynamical model for the evolution of a PWN inside a SNR, which we apply to G328.4+0.2 assuming it is a composite SNR (§4.1.1) or a PWN (§4.1.2). Finally, in §5 we summarize our results.

2. OBSERVATIONS

In this Section, we present the data gathered in a *XMM* observation (§2.1), a 1.4 GHz ATCA observation of G328.4+0.2 (§2.2), and a search for a radio pulsar in this source (§2.3).

2.1. X-ray Observations

On 2003 March 9–10, G328.4+0.2 was observed for ~ 50 ks by *XMM*. During this observation, the PN camera was operated in Small Window Mode, and the Mos1 and Mos2 camera were operated in Full Frame Mode. The “Thick” optical filter was used due to the presence of numerous bright stars in the field-of-view of G328.4+0.2. The data were reduced with the software package *XMM-SAS* v 6.0.0 with calibration files current through XMM-CCF-REL-174, using the standard procedure for reducing *XMM* data outlined in the *XMM-Newton ABC Guide*² and the *Birmingham XMM Guide*³.

2.1.1. Image Analysis

A vignetting corrected 0.2–12 keV image from the Mos1 and Mos2 instruments⁴, is shown in Fig. 1, in

which we observe three spatial components to the X-ray emission: a bright, compact feature located along the SW edge of the X-ray emission (“Clump 1”), a fainter, slightly extended feature located NE of the compact feature described above (“Clump 2”), and extended diffuse emission, roughly $1'$ in diameter, surrounding the two features described above (“Diffuse”). From the “Clump 1” region we detected 120 ± 12 counts above the background between 0.5–10 keV in the Mos1 detector and 136 ± 12 in the Mos2 detector, from the “Clump 2” region we detected 66 ± 9 counts in both the Mos1 and Mos2 detectors, and from the “Diffuse” regions we detected 360 ± 20 and 380 ± 20 counts from the Mos1 and Mos2 detectors, respectively.

We determined the spatial properties of these components using the *SHERPA* modeling software package (Freeman et al. 2001). Due to the low number of counts per pixel, we used the *simplex* fitting method and minimized the *cash* statistic (Cash 1979). We attempted to model Clump 1 and Clump 2 as circular 2D Gaussians, elliptical 2D Gaussians, or circular 2D Lorentzians, the latter of which is a good model for *XMM*’s point spread function (PSF; Ghizzardi & Molendi 2002). We attempted to model the Diffuse region as a circular or elliptical 2D Gaussian, and assumed a constant background. We fit the observed image to all model combinations of Clump 1, Clump 2, and Diffuse (attempts to eliminate one of these components resulted in significantly worse fits), and the best fit was obtained for a model in which Clump 1 is a 2D Lorentzian while Clump 2 and Diffuse are elliptical 2D Gaussians. The fit parameters for this model are given in Table 1, and the model and residuals are shown in Fig. 1, and from this conclude that the emission from Clump 1 is consistent with the PSF of *XMM*. Additionally, from this fit we estimate that Clump 1 and Clump 2 are separated by $\sim 10''$, while the centers of Clump 1 and Diffuse are separated by $\sim 15''$.

2.1.2. Spectral Results

In generating the spectra, only events with *FLAG* = 0 were used. Additionally, the event files were screened for background flares by binning the 10–15 keV light curve of each instrument by 50 s and then recursively flagging all bins with a count rate $> 3\sigma$ above the average. This procedure removed 3.0 ks, 2.3 ks, and 0.6 ks of data from the Mos1, Mos2, and PN detectors, respectively. Spectra were extracted for the regions shown in Fig. 1, and the resulting spectra were binned into a minimum of 25 counts per channel and modeled using *XSPEC* v12.2.0. The background regions used are also shown in Fig. 1.

To determine the composite spectra of G328.4+0.2, we jointly fit the spectrum obtained by the Mos1, Mos2, and PN detectors – shown in Fig. 2. The background-subtracted observed 0.5–10 keV count rate of G328.4+0.2 was 0.012 ± 0.001 counts s^{-1} in the Mos1 detector (555 ± 29 counts), 0.012 ± 0.001 counts s^{-1} in the Mos2 detector (580 ± 30 counts), and 0.045 ± 0.001 counts s^{-1} in the PN detector⁵ (1576 ± 63 counts). We fit the spectra to seven different models separately – a power-law, a blackbody, bremsstrahlung, a Raymond-Smith plasma, and a

² Available at <http://heasarc.gsfc.nasa.gov/docs/xmm/abc/>

³ Available at <http://www.sr.bham.ac.uk/xmm2/guide.html>

⁴ We did not use the PN data due to the substantially larger pixel size of this instrument.

⁵ The PN detector count rate does not account for 29% dead time since this instrument was operated in Small Window Mode.

power-law plus one of these three thermal models – all attenuated for interstellar absorption. Only the single-component models produced reasonable fits (reduced $\chi^2 \sim 1$), and the fitted parameters are presented in Table 2. Both the blackbody ($kT_{\text{BB}} \sim 1.7$ keV, $T_{\text{BB}} \sim 20$ MK) and the bremsstrahlung models ($kT \sim 9$ keV) require unrealistically high temperatures, especially if the X-rays are from a PWN as argued by Hughes et al. (2000). The derived parameters for the power law model are similar to that observed in other PWN (e.g. Gotthelf 2003), and agree well with the results obtained for G328.4+0.2 by Hughes et al. (2000). There is no evidence for thermal X-ray emission, which one would expect from a SNR, in this source.

Since the individual regions discussed in §2.1.1 did not have enough counts for spectral fitting, we measured their hardness ratio (HR), defined as:

$$HR = \frac{H - S}{H + S} \quad (1)$$

where H is the number of counts in the Hard (higher energy) band and S is the number of counts in the Soft (lower energy) band, of the regions discussed in §2.1.1 to determine if there were any spatial variations in the X-ray spectrum of G328.4+0.2. Using the X-ray spectrum as a guide, we calculate HR with H as the number of counts between 4 and 8 keV and S as the number of counts between 2 and 4 keV. Since the pixels on the PN detector are sufficiently large that it is not possible to separate the emission from these regions, we only use data from the MOS1 and MOS2 detectors. The calculated, background subtracted HR of G328.4+0.2 is 0.25 ± 0.04 , of the Clump 1 region is 0.29 ± 0.07 , of the Clump 2 region is 0.31 ± 0.11 , and of the diffuse region is 0.24 ± 0.05 (1σ errors). As a result, we conclude that there is no significant change in the X-ray spectrum of G328.4+0.2 between these features.

2.1.3. Timing Results

A clear signature for the presence of a neutron star would be the detection of X-ray pulsations in the emission from G328.4+0.2. We searched for this using the Z_n^2 test defined by Buccheri et al. (1983), where n is the harmonic number of periodic signal, for $n = 1, 2, 3, 4$. The maximum frequency searched was $\nu_{\text{max}} = 1/(2n\Delta t)$, the minimum frequency searched was $1/20$ Hz, and the frequency step was $1/4t_{\text{obs}}$ (5×10^{-6} Hz, oversampling the Nyquist rate by a factor of 2), where Δt is the time resolution of the dataset (5.7 ms) and t_{obs} is the length of the observation. We only used events from the PN instrument (5.7 ms since it was operated in Small Window Mode) due to the poor time resolution (2.6s) of the MOS data. Additionally, we only used events from the Clump 1 region because only only emission from the central NS should be pulsed and as the brightest X-ray region of G328.4+0.2, this region is the most probable location of any neutron star. Unfortunately, due to the large pixel size of the PN instrument this region is contaminated by emission from Clump 2 and the Diffuse region. The event times from the resultant event list were barycentered to the Solar System reference frame, and we searched for a periodicity over multiple energy ranges in order to maximize the sensitivity of our search. The most significant period detected was in the dataset which only

included photons between 5 and 10 keV (159 photons), in which for $n = 4$ a signal with period $P = 336$ ms had $Z_3^2 = 49.5$ in 2074786 independent trials for this value of n and energy range, which has a 12% chance of being a false positive, a $< 2\sigma$ result. Statistically, the most significant sinusoidal ($n = 1$) pulse was in the 1–20 keV dataset (340 photons), and had a period $P = 73.1$ ms with a $Z_1^2 = 34.4$ in 8365396 trials, a 34% chance of being a false positive. Assuming that this signal is not significant, we derive an upper limit on the pulse fraction of 45% for a sinusoidal pulse profile and 22.5% for a δ -function pulse profile (Leahy et al. 1983). Using the PN count rate and size of the Clump 2 and Diffuse regions, $\sim 1/3$ of the counts in the Clump 1 region is contamination from these regions. Accounting for this, we are only able to put an upper limit on the pulse fraction of 67% for a δ -function pulse profile. This upper limit is consistent with the pulse fraction observed from other young neutron stars.

2.2. Australia Telescope Compact Array Observations

Based on previous radio observations of G328.4+0.2, there was a dispute in the literature as to whether this source is a PWN, as argued by Gaensler et al. (2000), or a composite SNR, as argued by Johnston et al. (2004). The argument for this source being a PWN centered on the flat spectrum of the radio emission, as well as the high degree of polarization observed from the center (Gaensler et al. 2000), while the radial polarization angles observed at the edge of this is more consistent with a SNR (Johnston et al. 2004). If there is a SNR component in G328.4+0.2, we expect that some of the radio emission from this source should have a steep ($\alpha < -0.3$) spectrum. To search for such emission, we observed G328.4+0.2 for 12 hours at 1.4 GHz with the Australia Telescope Compact Array (ATCA) on 2005 June 25. Flux density calibration was carried out using an observation of PKS B1934-638, and phase calibration was carried out with regular observations of PMN J1603-4904. The observation was carried out using two 128 MHz bands, one centered at 1.344 GHz and the other at 1.432 GHz, and the data reduction was done using the MIRIAD software package. The observation was conducted when the ATCA was in the 6B configuration, which has a longest baseline of ~ 6000 m ($\sim 6''9$) and a shortest baseline of ~ 200 m ($\sim 3''.4$). As a result, this dataset alone is not sensitive to large-scale emission from G328.4+0.2. To improve the sensitivity to diffuse emission, we combined this dataset with the 1.4 GHz data used by Gaensler et al. (2000) as well as continuum data gathered in the Southern Galactic Plane Survey (McClure-Griffiths et al. 2005). Total intensity images from this combined dataset were formed using natural weighting, multi-frequency synthesis, and maximum entropy deconvolution. The final image, shown in Fig. 3, has a resolution of $7''.0 \times 5''.8$, and an rms noise of ~ 0.15 mJy beam $^{-1}$. The measured 1.4 GHz flux density of G328.4+0.2 is 13.8 ± 0.4 Jy – consistent with the value measured by Gaensler et al. (2000). For a 4.5 GHz flux of 12.5 ± 0.2 Jy (Gaensler et al. 2000), this implies that G328.4+0.2 has a radio spectral index $\alpha = -0.03 \pm 0.03$.

As seen in Fig. 3, the radio emission from G328.4+0.2 is very complicated, and contains multiple morphological features. The major features are:

- **Central Bar:** The Central Bar is the brightest morphological feature in G328.4+0.2, and has been previously detected at both 4.8 GHz (Gaensler et al. 2000) and 19 GHz (Johnston et al. 2004). The Central Bar runs roughly E-W, and the western edge of the bar is bifurcated, first noticed by Johnston et al. (2004). The length of the bar is $\sim 1'.75$ long, and inside the bar there are three peaks in the radio emission.
- **Filamentary Structure A:** These are the curved filaments near the center of G328.4+0.2 which appear to be connected to the Central Bar, the brightest of which is the “Y” shaped structure NE of the eastern edge of the Central Bar. In general, these filaments are more prominent on the eastern side of G328.4+0.2 and appear confined to the central region of G328.4+0.2, not extending much beyond the inner half.
- **Filamentary Structure B:** These are the faint, radial filaments predominantly found on the western side of G328.4+0.2, as shown in Fig. 4. The inner parts of these filaments are located $\sim 2'.5$ from the center of G328.4+0.2, and their length varies across G328.4+0.2 – in the southern half, two filaments appear to extend to the edge of the source while in the northern and western parts of G328.4+0.2 they are substantially shorter. While some of these filaments are kinked or curved, most are fairly straight and radial in orientation. These features were not detected by Gaensler et al. (2000) and Johnston et al. (2004) due to the insufficient u - v coverage of those observations.
- **Filamentary Structure C:** As shown in Fig. 3, these are features located near the outer edge of G328.4+0.2 that are parallel to the outer edge. These features are more prominent and more plentiful in the eastern half of G328.4+0.2.
- **Outer Protrusions:** The Outer Protrusions are faint features – the two most prominent of which are in the NE quadrant of G328.4+0.2 – that extend beyond the outer boundary of G328.4+0.2. Several of these structures have bow-shock morphologies.

The physical interpretation of these features will be presented in §3.2. It is worthwhile to note here that several of these morphological features (e.g. the Central Bar and the internal filamentary structures) have been observed in other PWNe such as MSH 15-56 (Dickel et al. 2000) and 3C58 (Slane et al. 2004), while others (e.g. the Filamentary Structure C and Protrusions) are more characteristic of SNRs, such as the Vela SNR (Bock et al. 1998).

This *XMM* observation also allows, for the first time, a comparison between the radio and X-ray morphology of G328.4+0.2. As shown in Fig. 3, there is a significant offset between the X-ray and the center of the radio emission, with Clump 1 located $\sim 80''$ from the center of the radio emission. Additionally, the extent of the X-ray emission is significantly smaller than that of the radio emission. A physical interpretation of the X-ray

morphology and its relation to the radio emission will be discussed in §3.2.

2.2.1. Spectral Index Map

The previous 1.4 GHz dataset had a resolution ($\sim 20''$) significantly worse than that of the 4.5 GHz data, and therefore is not suitable for determining if there are small scale changes in α inside G328.4+0.2. With these new, high-resolution 1.4 GHz observations, it was possible to make a spectral index map of G328.4+0.2 using our new 1.4 GHz data and the 4.5 GHz data presented by Gaensler et al. (2000) since these datasets have comparable u - v coverage. To detect any variation in α , we made a spectral tomography map of G328.4+0.2 (Katz-Stone & Rudnick 1997). To do this, we first produced a 1.4 GHz image of G328.4+0.2 from data matched in u - v coverage with the 4.5 GHz data, and then smoothed both the new 1.4 GHz image and the 4.5 GHz image to a resolution of $8''$ to account for the poorer resolution of the 1.4 GHz data. Finally, we produced a series of difference images ($I_{\text{diff},\alpha}$) using the following formula:

$$I_{\text{diff},\alpha} = I_{1.4} - I_{4.5} \left(\frac{1.4}{4.5} \right)^\alpha \quad (2)$$

where $I_{1.4}$ and $I_{4.5}$ are the 1.4 and 4.5 GHz images produced above. In this method, the spectral index of a region is determined by the spectral index at which it disappears from the difference image. As shown in Fig. 5, most of the radio emission from G328.4+0.2 has a spectral index between $\alpha \sim -0.1$ and $\alpha \sim +0.1$, while the outer edges of G328.4+0.2 have a steeper spectrum ($\alpha \sim -0.4$) than the center, particularly the western edge of G328.4+0.2. This steeper spectrum material is coincident with some of the Filamentary Structure C discussed in §2.2, but there are no spectral features associated with any of the other radio morphological features in G328.4+0.2 or with the X-ray emission. A physical interpretation of these results will be discussed in §3.2.

2.3. Search for the radio pulsar at Parkes

As part of a project to search for pulsar counterparts to all Galactic PWNe (e.g. Camilo et al. 2002a), on 2005 October 13 we observed G328.4+0.2 using the ATNF Parkes telescope in NSW, Australia. As for similar such work, we employed the central beam of the Parkes multibeam receiver at a central frequency of 1374 MHz, with 96 frequency channels across a total bandwidth of 288 MHz in each of two polarizations. The integration time was 24 ks, during which total-power samples were recorded every 0.25 ms for off-line analysis.

We analyzed the data with standard pulsar searching techniques using PRESTO (Ransom et al. 2002). We searched the dispersion measure range 0 – $2600 \text{ cm}^{-3} \text{ pc}$ (twice the maximum Galactic DM predicted for this line of sight by the Cordes & Lazio 2002 electron density model), while maintaining close to optimal time resolution. In our search we were sensitive to pulsars whose spin period could have changed moderately during the observation due to very large intrinsic spin-down. The search followed very closely that described in more detail in Camilo et al. (2006). We did not identify any promising pulsar candidate in this search.

Applying the standard modification to the radiometer equation, for an assumed pulsation duty cycle of 10%,

and accounting for a sky temperature at this location of 15 K, we were nominally sensitive to long-period pulsars having a period-averaged flux density at 1.4 GHz of $S_{1400} > 0.05$ mJy. In fact, this limit applies only to such long-period pulsars as to not be of practical interest for us: for a distance of ~ 17 kpc along this line of sight, the expected DM is $\approx 1200 \text{ cm}^{-3} \text{ pc}$, and the scatter-broadening of the radio pulses due to multipath propagation is expected to be ~ 50 ms at 1.4 GHz (Cordes & Lazio 2002). This would likely render pulsations undetectable from any short-period pulsar, such as we expect to power G328.4+0.2, regardless of average radio flux. We therefore repeated the search at a higher radio frequency ν , since the scattering timescale is approximately $\propto \nu^{-4}$.

On 2007 January 4 we observed G328.4+0.2 at Parkes at a central frequency of 3078 MHz, with 288 channels spanning a bandwidth of 864 MHz in each of two polarizations. The total-power samples were recorded every 1 ms for 30 ks, and analyzed in a manner analogous to that described previously for the 1.4 GHz data. This time a few somewhat-promising candidates were identified in the analysis, and a second 3 GHz observation was made, on 2007 March 19, for 36 ks. Analysis of this second observation did not confirm the original candidates, and we have therefore not detected any radio pulsar counterpart for the PWN in G328.4+0.2. The sensitivity of our 3 GHz observations was about 0.03 mJy for long-period pulsars ($P \gtrsim 20$ ms) and decreasing gradually for shorter periods. For the predicted DM, at this frequency the scattering timescale is expected to be ~ 2 ms, comparable to the dispersion smearing across each individual channel, ~ 1 ms. Propagation effects should therefore not have prevented the detection of signals with $P \gtrsim 5$ ms.

Converting the 3 GHz flux density limit to a frequency of 1.4 GHz, using a typical pulsar spectral index of -1.6 (Lorimer et al. 1995), results in $S_{1400} \lesssim 0.1$ mJy. For a distance of ~ 17 kpc, this corresponds to a pseudoluminosity limit of $L_{1400} \equiv S_{1400} d^2 \lesssim 30 \text{ mJy kpc}^2$. This is comparable to L_{1400} of the very young pulsars B1509–58, J1119–6127, and Crab (Camilo et al. 2002b), but a factor of about 60 greater than for the young pulsar in 3C58 (Camilo et al. 2002c), which has the smallest known radio luminosity among young pulsars. Based on these results, it is therefore entirely possible that G328.4+0.2 harbors an as-yet undetected young pulsar beaming toward the Earth with an ordinary radio luminosity.

3. INTERPRETATION OF X-RAY AND RADIO OBSERVATIONS OF G328.4+0.2

The X-ray spectrum of G328.4+0.2 is characteristic of PWNe (see Gotthelf 2003 for a compilation of the X-ray properties of PWNe), and therefore conclude that the X-ray emission from G328.4+0.2 comes from a PWN and not from a SNR. The same is true for the polarized, flat-spectrum radio emission detected from the center of G328.4+0.2 which are also characteristic of PWNe. Therefore, in the following discussion we assume that the X-ray and flat spectrum radio emission are both produced by a PWN. In §3.1, we discuss the evolutionary sequence of PWNe in SNRs and the observational signatures of each stage. In §3.2, we use the results from the observations presented in §2.1 and §2.2 to draw general

conclusion about the properties of G328.4+0.2.

3.1. Evolution of PWN in SNRs

Both PWNe and SNRs are dynamic objects, and when the PWN is inside the SNR its evolution is affected by the behavior of both the central neutron star and the surrounding SNR. While the PWN is inside the SNR, it typically goes through three evolutionary phases (Chevalier 1998; van der Swaluw et al. 2004):

- **The Free-Expansion Phase** – In this phase, the PWN freely expands into the cold material inside the SNR, sweeping up and shocking the surrounding ejecta into a thin shell (Chevalier & Fransson 1992; van der Swaluw et al. 2001). Since the PWN is confined only by the shock wave its expansion drives into the surrounding SNR, and the velocity of this shock wave is much larger than the neutron star velocity, it is free to move inside the SNR with the neutron star.
- **Collision with the Reverse Shock** – As the SN sweeps up and shocks the surrounding ambient material, a reverse shock (RS) is driven into the ejecta. Eventually, the PWN will encounter the RS, and as a result, can not continue to freely expand inside the SNR because it is no longer in an essentially pressureless environment. Initially, the pressure behind the RS is higher than the pressure inside the PWN, and as result the PWN is compressed. As it contracts, the pressure inside the PWN increases adiabatically and eventually will be higher than its surrounding, and will as a result re-expand inside the SNR (Blondin et al. 2001; Bucciantini et al. 2003; Reynolds & Chevalier 1984; van der Swaluw et al. 2001). Once the PWN encounters the RS, the expansion velocity of the PWN decreases significantly and falls below that of the neutron star, which is unaffected by this collision. As a result, the neutron star can detach itself from its PWN.
- **Relic PWN Phase** – When the neutron star detaches from the relic nebula, it forms a new PWN from the relativistic e^+/e^- plasma it continues to inject into the SNR (van der Swaluw et al. 2004). The PWN around the neutron star and relic nebula evolve differently. The relic nebula continues to contract/expand inside the SNR until it achieves pressure equilibrium with its surroundings, a process that can take many tens of thousands of years. The new PWN initially expands sub-sonically, but when the neutron star is $\sim 2/3$ of the way to the SNR shell, its velocity will become supersonic relative to the surrounding material and the PWN will take on a bow-shock morphology (van der Swaluw et al. 2004). Eventually, the neutron star will leave the SNR, and as it passes through the SNR shell it may re-energize the surrounding SNR material, as possibly observed in SNRs G5.4-1.2 and CTB80 (Shull et al. 1989).

As the PWN evolves inside the SNR, its appearance changes radically. During the Free-Expansion phase, the morphology of the PWN is determined by the properties

of the particle wind expelled by the neutron star. In these cases, the neutron star is in the center of the PWN, and there is no significant offset between the radio and X-ray emission from the PWN. In general, during this stage the PWN is located near the center of the observed SNR shell. Examples of PWNe in this evolutionary stage are the PWNe in SNR 0540-693 in the LMC (Reynolds 1985), as well as those in the Milky Way SNRs G11.2-0.3 (Roberts et al. 2003; Tam et al. 2002) and G21.5-0.9 (Matheson & Safi-Harb 2005).

Due to the offset in the PWN's position with respect to the SNR's center as a result of the neutron star's velocity or inhomogeneities in the ISM, it is expected that one side of the PWN will encounter the RS before the other side (Blondin et al. 2001; van der Swaluw et al. 2004). As a result, the PWN will no longer be symmetrically oriented around the neutron star (van der Swaluw et al. 2004), leading to an offset between the radio and X-ray emission from the PWN. Because the cooling time for X-ray producing electrons is very short compared to that of radio emitting electrons, the X-ray emission of a PWN is expected to be brightest at the current location of the neutron star while the radio emission reflects the effect of the RS on the PWN. The compression/re-expansion cycle triggered by the PWN/RS collision will also affect the appearance of the PWN. According to a spherically symmetric MHD simulation of a PWN in this phase, compression of the PWN by the RS leads to an overpressurized region forming in the center of the PWN. Material injected by the neutron star after this point is then confined to the small region, leading to the formation of a radio/infrared "hot spot" in the center of the PWN (Bucciantini et al. 2003).

The PWN/RS interaction also leads to the formation of hydrodynamic, primarily Rayleigh-Taylor (R-T), instabilities at the PWN/SNR interface (Blondin et al. 2001). During the PWN's initial free-expansion phase, the shell of material swept up by the PWN is subject to both thin shell and R-T instabilities (Bucciantini et al. 2004; Jun 1998), but the growth rate of these features is expected to be sufficiently small that the PWN is not disrupted, especially if even a small percentage of the total energy of the pulsar's wind is in magnetic fields (Bucciantini et al. 2004). However, during the PWN/RS interaction, rapid mixing of pulsar wind and SNR material is expected when the PWN re-expands into the SNR (Blondin et al. 2001). In fact, numerical simulations suggest that the PWN is disrupted after its first re-expansion into the SNR as a result of these instabilities (Blondin et al. 2001). It is important to note that these instabilities are only expected to affect the relic nebula and not the new PWN formed by the neutron star further from the SNR's center. Once the composite SNR enters the Relic PWN phase, the X-ray emission is expected to be dominated by the new PWN since it contains the high energy particles recently injected by the neutron star, while the radio emission is dominated by the relic nebula which contains most of the older particles that are expected to contribute at low frequencies. As a result, during this phase the radio-emitting electrons are expected to be dominated by electrons injected during the free-expansion phase, while the X-ray is from electrons injected after the passage of the RS.

3.2. Observational Results

In this Section, we use the results from the observations presented in §2.1 and §2.2, as well as the basic evolutionary sequence for PWN in SNRs described above in §3.1 to make some initial statements on the nature, evolutionary state, and properties of G328.4+0.2. The discussion given below is a very general interpretation of observed radio and X-ray features in G328.4+0.2, it provides a framework in which to test the various scenarios for G328.4+0.2 discussed in §4.1.1 and §4.1.2.

As mentioned in §1, there is a debate in the literature as to whether G328.4+0.2 is a PWN (Gaensler et al. 2000; Hughes et al. 2000) or a composite SNR (Johnston et al. 2004). In neither of the X-ray or radio observations presented above is there clear evidence (e.g. thermal X-ray emission or a bright, steep spectrum, radio shell) for a SNR component. If G328.4+0.2 is a composite SNR, then the outer boundary of the radio emission likely marks the outer radius of the SNR component, while the observed flat-spectrum radio emission and power law X-ray emission are emitted by the PWN. Using the extent of the flat-spectrum radio emission shown in Fig. 5 to estimate the size of the PWN component, we obtain that the radius of the PWN in this source must be $\gtrsim 2/3 R_{\text{G328}}$, the radius of G328.4+0.2. If G328.4+0.2 is a composite SNR, then Filamentary Structure 3, which as mentioned in §2.2.1 might have a steeper spectral index than the rest of the radio emission in G328.4+0.2, would be emission from the SNR. This emission is then possibly analogous to the corrugated structures seen in the NE part of the Tycho's SNR (Velazquez et al. 1998). Additionally, in this case the Outer Protrusions mentioned in §2.2 maybe are ejecta "bullets", similar to those observed in the Vela SNR (Aschenbach et al. 1995) and SNR N63A (Warren et al. 2003).

If G328.4+0.2 is a PWN, then the outer boundary of the radio emission is the outer radius of the PWN and the SNR in which it resides is undetected, similar to the case for the Crab Nebula. As a result, the steep spectrum radio emission seen at the edge of G328.4+0.2, as well as Filamentary Structure C and the Outer Protrusions observed in the radio, correspond to material swept-up by the PWN. This is because radio emission from the pulsar wind is observed to have a flat spectrum, unlike this material. As a result, Filamentary Structure C, as well as the radial component seen by Johnston et al. (2004) in the polarization angle along the outer edge of G328.4+0.2, are the result of the hydrodynamical (HD) instabilities at the PWN/SNR interface. Since these instabilities only occur when the PWN is accelerating the shell of swept-up material surrounding it, the current pressure inside the PWN (P_{pwn}) must be higher than that of the SNR material just of the PWN [$P_{\text{snr}}(R_{\text{pwn}})$]. Additionally, in this case the Outer Protrusions would be the result of the PWN currently expanding into a clumpy medium (e.g. the PWN analog of the process described for young SNR by Jun et al. 1996), which requires that the expansion speed of the PWN, v_{pwn} , is currently positive. In this case, it is possible that the SNR surrounding G328.4+0.2 will be detected at a later date, as was the case for G21.5-0.9 (Matheson & Safi-Harb 2005).

Regardless of whether G328.4+0.2 is a composite SNR

or a PWN, the offset between the radio and X-ray emission from the PWN component implies that the PWN/RS collision has already occurred. The Central Bar is then the remains of the over-pressurized region created when the PWN was compressed by the RS, with the bar-like shape of this region the result of either an asymmetric RS or the anisotropic wind emitted by the neutron star. The Central Bar should then consist of pulsar wind material, which accounts for the $\alpha \sim 0$ spectral index of this region as shown in Fig. 5. Additionally, the flat spectral index observed from Filamentary Structures A implies that this feature is emitted by pulsar wind material. As mentioned in §3.1, when the PWN re-expands after the initial compression by the RS, numerical simulations suggest that the rapid mixing of the SNR ejecta and pulsar wind material can then occur. In their 2D simulations of this process, Blondin et al. (2001) observe features similar to that of Filamentary Structure A, and as a result we conclude that the existence of these features requires that the PWN has re-expanded at least once after its initial compression by the RS. Since the radius of flat-spectrum radio emission from G328 is larger than the outer radius of Filamentary Structure A, the instabilities formed during this expansion must not have completely disrupted the PWN. This differs from the results of Blondin et al. (2001), in which the PWN is disrupted during the first re-expansion. This is most likely due to the damping effect of the PWN's magnetic field on Raleigh-Taylor instabilities, which is not accounted for by Blondin et al. (2001).

Finally, we discuss the X-ray emission seen from G328.4+0.2 which, based on its X-ray spectrum, is emitted by pulsar wind material. The observed offset between Clump 1, Clump 2, and the Diffuse regions of the X-ray emission implies that the PWN is not freely expanding, consistent with the explanation that the PWN has collided with the RS. We identify Clump 1 as the current location of the neutron star since it is the brightest X-ray feature, Clump 2 as the location of the termination shock in the PWN (Kennel & Coroniti 1984), and the Diffuse emission is produced by recently injected plasma streaming away from the neutron star. In this case, the extent of the Diffuse component depends on the synchrotron lifetime of the X-ray emitting particles in the PWN.

The X-ray emission also provides an estimate of the physical properties of the central neutron star, namely a measure of the neutron star's rotational spin-down energy, \dot{E} . A comparison of observed X-ray luminosity L_x and \dot{E} shows a trend that neutron stars with a higher L_x have a higher \dot{E} , and that the relationship between these two quantities is (Possenti et al. 2002):

$$\log L_{X,(2-10)} = 1.34 \log \dot{E} - 15.34 \quad (3)$$

where $L_{X,(2-10)}$ is the X-ray luminosity of the source between 2 and 10 keV, albeit with a significant scatter (Possenti et al. 2002). For the absorbed power-law fit to the X-ray emission from G328.4+0.2 given in Table 2, the unabsorbed 2–10 keV flux of G328.4+0.2 is $\sim 1 \times 10^{-12}$ ergs cm $^{-2}$ s $^{-1}$. For a distance to G328.4+0.2 of $d = 17d_{17}$ kpc, we obtain that:

$$L_{X,(2-10)} \sim 3.5d_{17}^2 \times 10^{34} \text{ ergs s}^{-1}, \quad (4)$$

which, using Eq. (3), gives us an estimate of \dot{E} :

$$\dot{E} \sim 1.7d_{17}^{1.49} \times 10^{37} \text{ ergs s}^{-1}. \quad (5)$$

This number is somewhat less than estimate obtained by Gaensler et al. (2000) ($\dot{E} = 8.3 \times 10^{38}$ ergs s $^{-1}$), who assumed that $\dot{E} = 4 \times 10^{-4} L_R$, where L_R is the radio luminosity of G328.4+0.2. Our estimate of \dot{E} is similar to the estimate by Hughes et al. (2000) ($\dot{E} \sim 10^{37} - 2 \times 10^{38}$ ergs s $^{-1}$), who also used the $L_x - \dot{E}$ relation.

4. SIMPLE HYDRODYNAMIC MODEL FOR THE EVOLUTION OF A PWN INSIDE A SNR

In order to determine what neutron star, SN, and ambient density properties are required to produce a system with these properties described in §3.2, we have developed a simple hydrodynamic (HD) model for the evolution of a PWN inside of a SNR, which we then apply to G328.4+0.2 in §4.1. This model is based largely on the models developed by Blondin et al. (2001) and van der Swaluw et al. (2001). The main goal of this model is to determine the radius of the PWN, R_{pwn} , as it progresses through the evolutionary sequence described in §3.1. In this model, we assume that the PWN can be treated as a perfect gas with adiabatic index $\gamma = 4/3$ and that is expanding into a SNR filled with a perfect gas with adiabatic index $\gamma = 5/3$. We also assume that the material swept-up by the PWN initially lies in a thin shell with inner radius $R = 23/24 R_{\text{pwn}}$ (van der Swaluw et al. 2001), as shown in Fig. 6. The dynamics of this mass shell are determined by the difference in pressure between the PWN and SNR, and by calculating the radius of this mass shell we determine $R_{\text{pwn}}(t)$. Once the PWN enters the Relic PWN phase of its evolution, this model only determines the properties of the relic nebula. What follows is a brief qualitative description of the model used, while the full suite of equations used to implement it quantitatively can be found in Appendix A.

As mentioned above, we model $R_{\text{pwn}}(t)$ by calculating the outer radius of the mass shell swept up by the PWN, ignoring the effect of any instabilities which could disrupt this shell. We solve for $R_{\text{pwn}}(t)$ by assuming that we know the values for the relevant quantities at a time $t - \Delta t$, and then calculate them for a time t , since the relevant equations can not be solved at all times analytically. we wrote a program in IDL to implement this numerically using the following procedure:

1. Calculate $R_{\text{pwn}}(t + \Delta t)$ by assuming that the mass shell around the PWN between t and $t + \Delta t$ moves with a constant velocity $v_{\text{pwn}}(t)$.
2. Calculate the internal energy of the PWN, $E_{\text{pwn}}(t + \Delta t)$, using the first law of thermodynamics:

$$\Delta E_{\text{pwn}} = \dot{E}t - P_{\text{pwn}}\Delta V_{\text{pwn}} \quad (6)$$

which takes into account energy losses from the adiabatic expansion/contraction of the PWN as well as any energy input from neutron star into the PWN between t and $t + \Delta t$ if the neutron star is still inside the PWN. Since we assume the PWN is filled with a $\gamma = 4/3$ perfect gas, $E_{\text{pwn}} \propto P_{\text{pwn}}V_{\text{pwn}}$ from the ideal gas law, where P_{pwn} is the internal pressure of the PWN and V_{pwn} is the volume of the PWN, as defined in Equations (A5 and (A6). Since $V_{\text{pwn}} \propto R^3$, and $\gamma = 4/3$ requires that

$P_{\text{pwn}} \propto V_{\text{pwn}}^{-4/3}$, we derive that $P_{\text{pwn}} \propto R^{-4}$. As a result, if there is no input from the neutron star, then $E_{\text{pwn}} \propto R_{\text{pwn}}^{-1}$. The energy input from the neutron star (ΔE_{psr}) is calculated by integrating Eq. (A7) between t and $t + \Delta t$.

3. Calculate $P_{\text{pwn}}(t + \Delta t)$ using Equations (A5) and (A6).
4. Calculate the pressure inside the SNR (P_{snr}), the density inside the SNR (ρ_{ej}), the velocity of the material inside the SNR (v_{ej}), and the sound speed of the material inside the SNR (c_s), at the outer radius of the PWN, $R = R_{\text{pwn}}(t + \Delta t)$ using a model for the evolution and structure of a SNR, as described in Appendix A.
5. If the PWN is expanding faster than the SNR material around it, increase the mass of the shell surrounding the PWN, $M_{\text{sw,pwn}}(t + \Delta t)$, accordingly, as described in Appendix A.
6. Calculate the force on the mass shell surrounding the PWN, $F_{\text{pwn}}(t + \Delta t)$, using Eqs. (A14) and (A15). During the initial free-expansion of the PWN inside the SNR, these equations reduce to Equation A4 of van der Swaluw et al. (2001) and Equation 14 of Chevalier (2005).
7. Calculate the new velocity of the mass shell around the PWN, $v_{\text{pwn}}(t + \Delta t)$, assuming that any mass swept up by the PWN between t and $t + \Delta t$ is done so inelastically:

$$v_{\text{pwn}}(t + \Delta t) = \frac{M_{\text{sw}}(t)v_{\text{pwn}}(t) + F_{\text{pwn}}(t + \Delta t)\Delta t}{M_{\text{sw}}(t + \Delta t)} \quad (7)$$

This is believed to be a reasonable approximation because the newly swept-up material is shocked by the mass shell and, as a result, its pre-existing momentum is transferred to the internal energy of the mass shell.

This model assumes that both the SNR and PWN are spherically symmetric, the PWN remains centered on the center of the SNR at all times, the PWN has no effect on the evolution of the SNR, and that the material swept-up by the PWN is incompressible and has a negligible internal pressure. Additionally, this model ignores the effects of magnetic field (Bucciantini et al. 2003) and RT instabilities at the PWN/SNR interface (Blondin et al. 2001; van der Swaluw et al. 2004) on the properties of the PWN. Despite these simplifications, our model does a reasonably good job of reproducing the results for Model A in Blondin et al. (2001), as shown in Fig. 7. In general, relative to results of Blondin et al. (2001) and other authors, our model tends to result in larger oscillations in $R_{\text{pwn}}/R_{\text{snr}}$ and a larger initial compression. The first discrepancy results from neglecting the effect of instabilities at the PWN/SNR interface that damp these oscillations, and the second from not including the effect of reflected shocks that enter the PWN at the time of the PWN/RS collision (Blondin et al. 2001). Additionally, we find that scenarios with the same total amount of energy deposited by the neutron star into the PWN, E_{psr} but with different neutron star properties

(e.g. different values of P_0 and B_{ns}) produce the same behavior of $R_{\text{pwn}}(t)$. This is different than the conclusion of Blondin et al. (2001), and believe that this discrepancy is the result of using a more realistic expression for \dot{E} , Eq. (A7), than a step function, the form used by Blondin et al. (2001).

4.1. Application of Model to G328.4+0.2

In the following discussion, we use the model given in §4 for a PWN's evolution inside a SNR to examine the different possibilities for the nature of G328.4+0.2 given in §3.2. We first analyze the possibility that G328.4+0.2 is a composite SNR (§4.1.1), and then the possibility that G328.4+0.2 is a PWN (§4.1.2). This model requires six inputs: the characteristic timescale of the neutron star's spin-down, τ_0 , initial spin-down power of the neutron star \dot{E}_0 , the velocity of the neutron star, v_{ns} , the kinetic energy of the SN ejecta E_{sn} , the mass of the SN ejecta M_{ej} , and the number density of the surrounding material n . In order to calculate these values, we use the following information:

- The distance to G328.4+0.2 is 17 kpc ($d_{17} \equiv 1$), which is the lower limit on the distance to this source as determined by Gaensler et al. (2000) using H I absorption. This implies that the current radius of G328.4+0.2 is $R_{\text{G328}} \equiv 12.5$ pc.
- The neutron star inside G328.4+0.2 is spinning down with a braking index $p = 3$, the braking index produced by a pure dipole surface magnetic field. Additionally, we assume that the neutron star's moment of inertia is $I = 10^{45}$ g cm², the value derived for standard equations of state for a neutron star (Shapiro & Teukolsky 1983). Both of assumptions are standard in the literature (e.g. Blondin et al. 2001).
- The offset between the Clump 1, which as described in §3.2 is believed to be the location of the neutron star powering the PWN, and the center of the radio emission is due to neutron star's spatial velocity, v_{ns} . Using §2.1.1, we determine that this observed offset corresponds to physical distance of $\sim 6.6d_{17}$ pc. Since the observed offset is due only to the neutron star's velocity in the plane of the sky, it is a lower limit on the true distance the neutron star has traveled since the SN explosion, r_{ns} . If we assume that $v_{\text{ns}} = r_{\text{ns}}/t_{\text{now}}$, where t_{now} is the age of G328.4+0.2, the observed offset allows us to estimate the minimum spatial velocity of the neutron star, $v_{\text{ns}}^{\text{min}}$, equal to:

$$v_{\text{ns}}^{\text{min}} = \frac{6.6d_{17} \text{ pc}}{t_{\text{now}}} \quad (8)$$

- Using Equation (A19), we determine that for standard initial periods ($P_0 \sim 5 - 20$ ms) and magnetic field strengths ($B_{\text{ns}} = 5 \times 10^{11} - 10^{13}$ G), τ_0 varies from $\sim 100 - 2000$ years. To cover this range, we assume that τ_0 of the neutron star in G328.4+0.2 can have one of three different values:

$$\tau_0 = 430, 770, \text{ and } 1730 \text{ years.} \quad (9)$$

which respectively correspond to a neutron star with $B = 10^{12}$ G and $P_0 = 5$ ms, $B = 3 \times 10^{12}$ G

and $P_0 = 20$ ms, or $B = 5 \times 10^{11}$ G and $P_0 = 5$ ms. This range of τ_0 is similar to those used by Blondin et al. (2001), van der Swaluw et al. (2001), and Bucciantini et al. (2003).

- G328.4+0.2 is expanding into a uniform medium ($s = 0$ in the notation of Chevalier 1982). This assumes G328.4+0.2 is much larger than either the main sequence and late-stage wind bubble formed by its progenitor, both of which are expected to have an interior $\rho \propto r^{-2}$ density structure. While the typical size of these structures is smaller than R_{G328} , this is not the case for very massive stars ($M \gtrsim 15 M_\odot$) for which these bubbles can reach sizes of ~ 100 pc or larger in low density ($n \lesssim 1 \text{ cm}^{-3}$) environments (Chevalier & Emmering 1989; Chevalier & Liang 1989). In this case, our assumption of a constant density medium would not be correct. However, the effect of G328.4+0.2 still being inside a stellar wind bubble since this does not significantly modify the evolution of the SNR. Since there is no *a priori* information on the density around G328.4+0.2, we assume it is one of the following values:

$$\log n = -1.5, -1.0, 0, 0.5 \text{ cm}^{-3}. \quad (10)$$

which cover the range of densities in the warm ionized medium and the warm neutral medium.

- The ejecta mass of the SN explosion that formed G328.4+0.2, M_{ej} has one of the following values:

$$M_{\text{ej}} = 1, 5, 10 M_\odot \quad (11)$$

and that the kinetic energy of the ejecta, E_{sn} is:

$$\log(E_{\text{sn}}/10^{51} \text{ ergs}) = -0.5, 0, 0.5. \quad (12)$$

This range of M_{ej} and E_{sn} incorporate the range inferred from observations of “normal” SNe, but do not include hypernovae.

- We assume that the $L_x - \dot{E}$ relationship used in §3.2 is accurate to better than two orders of magnitude. As a result, in §4.1.1, we assume that the current spin-down luminosity of the neutron star in G328.4+0.2 is one of the following:

$$\dot{E} = 0.017, 0.17, 1.7, 17, \text{ and } 170 \times 10^{37} \text{ ergs s}^{-1}, \quad (13)$$

and in §4.1.2 assume that $1.7 \times 10^{35} < \dot{E} < 1.7 \times 10^{39} \text{ ergs s}^{-1}$.

These are the initial conditions used in both §4.1.1 and §4.1.2. The remaining input parameters into the model are the initial spin-down luminosity \dot{E}_0 and space velocity v_{ns} of the neutron star, and the method for determining the possible values of these parameters is given in §4.1.1 and §4.1.2. Finally, for all trials discussed in §4.1.1 and §4.1.2 the model begins at a time $t = 0.5$ years, with $\Delta t = 0.5$ years.

4.1.1. G328.4+0.2 as a Composite SNR

In this Section, we evaluate the possibility that G328.4+0.2 is a composite SNR. To do this, we first assume that the outer edge of the radio emission from

this source denotes the edge of the SNR, and therefore $R_{\text{G328}} \equiv R_{\text{snr}}$. As a result, for a given value of E_{sn} , M_{ej} , and n , we use the model for the evolution of a SNR discussed in Appendix A to calculate the current age of G328.4+0.2, t_{now} . With this value of t_{now} and assumed values for the current spin-down luminosity of the neutron star, \dot{E} , and τ_0 , we are able to calculate both the initial spin-down luminosity \dot{E}_0 and initial period P_0 of the neutron star in G328.4+0.2 using Eqs. (A7) and (A9), respectively.

Using this procedure, we ran our model using all possible combinations of the input parameters (τ_0 , \dot{E} , E_{sn} , M_{ej} , and n) given in §4.1, for a total of 540 different combinations. To see which combination of these input parameters provide a plausible explanation for G328.4+0.2, we require the following:

- **Criterion 1:** $v_{\text{ns}}^{\text{min}} < 2000 \text{ km s}^{-1}$, since a neutron star with a higher velocity than this is extremely implausible based on pulsar observations (Hobbs et al. 2005).
- **Criterion 2:** $P_0 > 2$ ms, the minimum rotation period of a young proto-neutron star before it breaks up (Goussard et al. 1998).
- **Criterion 3:** The PWN is smaller than the SNR for all $t < t_{\text{now}}$. While it is possible that PWN could expand to fill the entire SNR, it is not considered likely, and is contrary to the model assumption that the PWN does not affect the evolution of the SNR. Additionally, we also require that $R_{\text{pwn}}(t_{\text{now}}) \geq 0.67 R_{\text{snr}}(t_{\text{now}})$, due to the large observed size of the flat-spectral index radio emission which is produced from the PWN, as described in §3.2.
- **Criterion 4:** G328.4+0.2 is currently in the Free-Expansion or Sedov-Taylor phase of its expansion, i.e. $t_{\text{now}} < t_{\text{rad}}$, where t_{rad} , the age when a SNR goes radiative, is defined in Eq. A4. Once a SNR has entered its Radiative phase, it is expected that the radio emission from the SNR be confined to thin, bright, filaments like those observed in SNR G6.4-0.1 (Mavromatakis et al. 2004) – which are not observed in G328.4+0.2, or that the SNR is radio-quiet.
- **Criterion 5:** The PWN/RS collision has already occurred, as described in §3.2, and the PWN has been compressed as a result of its collision with the RS. This is required to explain the Central Bar, as described in §3.2. This requires that $v_{\text{pwn}} < 0$ at some point in the past – which can only occur at a time $t > t_{\text{col}}$, the time when the PWN and RS collide.
- **Criterion 6:** The Central Bar created by the compression is still observable. This is satisfied if either the PWN is currently being compressed, $v_{\text{pwn}}(t_{\text{now}}) < 0$, or if the compression ended sufficiently recently such that it can be observed. The Central Bar is believed to be formed by both a pressure and a magnetic field enhancement at the center of the PWN (Bucciantini et al. 2003). As a

result its observable lifetime is the synchrotron lifetime of electrons accelerated by the magnetic field enhancement. Therefore, we assume that the lifetime of the central bar is the synchrotron age of the accelerated electrons, τ_{synch} , equal to:

$$\tau_{\text{synch}} = 3 \times 10^4 \nu^{-1/2} B_{\text{pwn}}^{-3/2} \text{ years}, \quad (14)$$

where ν is the observed frequency, in units of Hz, and B_{pwn} is the strength of the magnetic field inside of the PWN, in units of G. With this information, in the case that $v_{\text{pwn}}(t_{\text{now}}) > 0$ we determine if the central bar is still observable by evaluating τ_{synch} at 22 GHz (since this is the highest frequency at which the Central Bar is observed; Johnston et al. 2004) at the time when the compression ends, assuming that B_{pwn} can be derived using the minimum energy estimate. This criterion is satisfied if $\tau_{\text{synch}} > t_{\text{now}} - t_{\text{re-exp}}$, where $t_{\text{re-exp}}$ is the time when the compression phase ends.

That the above criteria fall into two categories: criteria required for physical plausibility (Criteria 1–3) and those which depend on our interpretation of the radio and X-ray properties of G328.4+0.2 (Criteria 4–6).

Of the 540 possible combinations of the input parameters, only one passes all six criteria. The predicted SNR, PWN, and neutron star properties of this scenario are given in Table 3, and the behavior of R_{pwn} as a function of time is given in Figure 8. In this scenario, G328.4+0.2 is quite young, ~ 4900 years old, and the energy injected into the SNR by the neutron star is similar to the kinetic energy of the SN explosion ($\sim 10^{51}$ ergs). However, in this scenario, as shown in Fig. 8, the predicted compression is very small; when the compression begins, $R_{\text{pwn}} = 3.838$ pc, and when the PWN begins to re-expand into the SNR, $R_{\text{pwn}} = 3.834$ pc. This small decrease is not surprising given that, as shown in Table 3, the total energy inputted into the PWN by the pulsar (E_{psr}) is very close to the kinetic energy of the SN ejecta (E_{sn}). This negligible decrease in the volume of the PWN is unlikely to form a central bar as prominent as the one observed (Fig. 3), and therefore we feel is unlikely to be the correct explanation for G328.4+0.2.

4.1.2. G328.4+0.2 as a PWN

In order to evaluate if G328.4+0.2 is a PWN, we use the model presented in §4 to determine the earliest time⁶ (t_{now}) at which a PWN powered by a neutron star with a given initial period P_0 reaches the observed size of G328.4+0.2 ($R_{\text{pwn}} = 12.5$ pc) if it is expanding into as yet unseen SNR formed by ejecta with initial mass M_{ej} and kinetic energy E_{sn} which exploded in a constant-density ambient medium with number density n . To consider all reasonable cases, we ran our model using all combinations of the values of τ_0 , E_{sn} , M_{ej} , and n given in §4.1, as well as $P_0 = 5, 10, 25, 100$ ms for a total of 432 different trials. In this scenario, since it is not possible to determine an independent estimate of the age of the system, it is necessary to assume a value of P_0 . To determine which of these combinations are possible explanations for G328.4+0.2, we required that:

⁶ Due to oscillations in radius the PWN undergoes after its collision with the RS, it can reach the current size at multiple times.

- **Criterion 1:** $v_{\text{ns}}^{\text{min}} < 2000 \text{ km s}^{-1}$. Since, in this scenario, we have no prior estimate of the age of G328.4+0.2, when we run our model we assume that $v_{\text{ns}} = 0$. This does not effect our results because r_{ns} , as measured in §4.1, is less than $R_{\text{pwn}} \equiv R_{\text{G328}}$, and therefore the neutron star is always injecting energy into the PWN as it does if $v_{\text{ns}} = 0$. Once, for a given set of input parameters we have determined t_{now} , we calculate $v_{\text{ns}}^{\text{min}}$ using Equation (8).
- **Criterion 2:** The current spin-down energy of the neutron star in G328.4+0.2 is between $0.017 \leq E_{37} \leq 170$, where $E_{37} \equiv \dot{E}/10^{37}$ ergs. This is based on the work done in §3.2, and is consistent with the initial values of \dot{E} used in §4.1.1. Since in this scenario we have no estimate of the age of G328.4+0.2, we are unable to assume a value for \dot{E} of the central neutron star and then calculate its initial spin-down luminosity, as we did in §4.1.1.
- **Criterion 3:** $R_{\text{pwn}} < R_{\text{snr}}$ for all times $t < t_{\text{now}}$, as explained in §4.1.1.
- **Criterion 4:** The PWN has already collided, and has been compressed by, the RS, as explained in §3.2.
- **Criterion 5:** The Central Bar created by the compression of the PWN is still observable. The method of determining if this is satisfied is the same as the one used in §4.1.1.
- **Criterion 6:** The PWN must have been able to form RT instabilities after the PWN/RS collision. As in §4.1.1, we implement this requirement by requiring that $P_{\text{pwn}} > P_{\text{snr}}(R_{\text{pwn}})$ for some $t > t_{\text{col}}$. Additionally, as explained in §3.2, in order for the PWN to create Filamentary Structure C it must currently be unstable to R-T instabilities – requiring that $P_{\text{pwn}} > P_{\text{snr}}(R_{\text{pwn}})$ now.
- **Criterion 7:** As explained in §3.2, the observed Outer Protrusions in the radio require that the PWN currently be expanding into the SNR, $v_{\text{pwn}}(t_{\text{now}}) > 0$.
- **Criterion 8:** G328.4+0.2, must have only undergone one compression/re-expansion cycle. As explained in §3.2, numerical simulations of PWN inside SNRs finds that the PWN is disrupted after the first such cycle (Blondin et al. 2001).

It is important to note that, if G328.4+0.2 is a PWN, then the radio and X-ray observations provide little information on the evolutionary phase of the (unseen) SNR and no information on the current ratio of the PWN and SNR radii.

Out of the 432 possible combinations of the input parameters, only five satisfy all ten of the above criteria, as listed in Table 4. While the neutron star appears to be inside the PWN, it is possible that this is just a projection effect. To evaluate the possibility that the PWN in G328.4+0.2 has already entered the Relic PWN phase of its evolution, we calculated $v_{\text{ns}}^{\text{min,II}}$, defined as:

$$v_{\text{ns}}^{\text{min,II}} = \frac{R_{\text{G328}}}{t_{\text{now}}}. \quad (15)$$

If $v_{\text{ns}} > v_{\text{ns}}^{\text{min,II}}$, then the G328.4+0.2 is a Relic PWN, if not, then it is still in the Collision with the RS phase of its evolution.

As shown in this Table, the predicted properties of G328.4+0.2 vary substantially if G328.4+0.2 is inside a Sedov or Radiative SNR. In the Sedov case, G328.4+0.2 is quite young, and progenitor SN explosion had a normal explosion energy but a low ejecta mass ($M_{\text{ej}} \sim 1 M_{\odot}$), and it occurred in a low density environment. Additionally, the neutron star formed in this explosion was spinning rapidly, has a low surface magnetic field strength ($B_{\text{ns}} < 10^{12}$ G), and a high space velocity ($v_{\text{ns}} \gtrsim 800 \text{ km s}^{-1}$). In the Radiative Case, G328.4+0.2 is substantially older, and the progenitor SN explosion was a low kinetic energy ($E_{\text{sn}} \sim 3 \times 10^{50}$ ergs) and high ejecta mass expanding. The neutron star in this case was born spinning somewhat slower and has a normal magnetic field strength for a young neutron star.

With the information presented in Table 5, it is possible to further refine the expected SNR and PWN properties. As argued in §4.1.1, the prominence of the central bar argues that, during the compression stage, the volume of the PWN decreased significantly. Though it is not possible at this time to quantify the compression needed, an examination of Table 5 shows that for only two models, ST 2 and Rad 1, did the volume of the PWN decrease by more than 10% – and therefore these two models are the most probable descriptions of G328.4+0.2. In the case of Rad 1, $v_{\text{ns}}^{\text{min,II}} \sim 100 \text{ km s}^{-1}$ is significantly less than the average neutron star velocity, $v \sim 400 \text{ km s}^{-1}$ (Faucher-Giguère & Kaspi 2006; Hobbs et al. 2005), implying that the PWN is in the Relic PWN phase of its evolution. Since the sound speed inside a Radiative SNR is quite low, $\sim 100 \text{ km s}^{-1}$, we expect that the PWN in the Rad 1 scenario would have a bow-shock morphology. Since there is no clear evidence for this in the X-ray or radio emission from G328.4+0.2, this suggests that ST 2 is a better fit to the data.

The conclusion that ST 2 is an accurate description of G328.4+0.2 is supported by circumstantial evidence as well. For this scenario, the expected radius of the termination shock around the neutron star, r_{ts} , defined as (Slane et al. 2004):

$$r_{\text{ts}}^2 = \frac{\dot{E}}{4\pi c P_{\text{pwn}}}, \quad (16)$$

assuming a spherical wind, is $r_{\text{ts}} \sim 0.6 \text{ pc}$, which corresponds to an angle of $\theta_{\text{ts}} \sim 8d_{17}''$ – a distance which is comparable to the offset between Clump 1 and Clump 2 derived in §2.1.1. Another interesting feature for this model is that, as shown in Fig. 4, the radius of the PWN at the time of re-expansion is similar to that of the outer parts of the central filamentary structures discussed in §2.2. While this correlation might be coincidental, this could imply that the hydrodynamic instabilities formed at the PWN/SNR interface during the re-expansion disrupted the shell of material swept up by the PWN – consistent with the simulation of Blondin et al. (2001). While not definitive, these two pieces of evidence argue that ST 2 is a reasonable description of G328.4+0.2.

The properties of ST 2 are given in Table 6, and the evolution of R_{pwn} is shown in Fig. 9. It is interesting to note that in this scenario, the PWN collides with the RS at a time $t_{\text{col}} < \tau_0$ ($t_{\text{col}} \approx 850$ years) so energy injection

by the neutron star into the PWN after the PWN/RS collision is important to the PWN’s evolution during this stage. It is important to note that this model predicts that the neutron star powering G328.4+0.2 is the most energetic neutron star in the Milky Way, as well as one of the fastest. Given that G328.4+0.2 is largest and has the highest radio luminosity of any known PWN, it is not surprising that it was formed by such a powerful neutron star. Finally, the age and \dot{E} predicted by this method are similar to those predicted by Gaensler et al. (2000).

In order to better understand the limitations of the approach in determining the properties of the neutron star and SNR in G328.4+0.2, we have run the model presented in §4 over a finer grid of parameters and evaluated the resulting PWN evolution using the same criteria as above. In Fig. 10, we show which values of P_0 and B_{ns} pass all of this criteria for three different kind of SN explosions: $E_{\text{sn}} = 10^{51}$ ergs and $M_{\text{ej}} = 1 M_{\odot}$, $E_{\text{sn}} = 3 \times 10^{51}$ ergs and $M_{\text{ej}} = 1 M_{\odot}$, and $E_{\text{sn}} = 4 \times 10^{51}$ ergs and $M_{\text{ej}} = 3.25 M_{\odot}$, assuming an ambient density with $n = 0.03$. The first set of SN parameters corresponds to ST 1, the second to ST 2, and third to a higher ejecta mass SN explosion is compatible with a neutron star with the same parameters as ST 2. For the first case, we find that a wide range of P_0 values are allowed but that $B_{\text{ns}} \lesssim 10^{12}$ G. In fact, for this set of SN parameters a $P_0 \sim 10$ ms, $B_{\text{ns}} \sim 8 \times 10^{11}$ G neutron star results in a PWN which is compressed a similar amount as in ST 2. In the second case, we find that P_0 and B_{ns} are tightly constrained around $P_0 \approx 5$ ms and $B_{\text{ns}} \approx 5 \times 10^{11}$ G. In the third set of SN parameters, we find that $P_0 \lesssim 6$ ms, but that B_{ns} spans a wide range of values, $\sim 10^{11} - 2 \times 10^{12}$ G.

To determine the allowed values of E_{sn} and M_{ej} , we followed the same procedure as above using two different sets of neutron star parameters: $P_0 = 5$ ms and $B_{\text{ns}} = 5 \times 10^{11}$ G (the neutron star parameters in the ST 1 and ST 2 scenarios), and $P_0 = 10$ ms and $B_{\text{ns}} = 8 \times 10^{11}$ G. For the first case, only models with $E_{\text{sn}} \sim 1 - 4 \times 10^{51}$ ergs and $M_{\text{ej}} \sim 0.5 - 3.5 M_{\odot}$ satisfy the criteria above – though a substantial compression of the PWN requires $E_{\text{sn}} \gtrsim 2 \times 10^{51}$ ergs. In the second case, we find that only models with $E_{\text{sn}} \lesssim 10^{51}$ ergs and $M_{\text{ej}} \sim 0.5 - 3.5 M_{\odot}$ are allowed.

While this error analysis shows that the method used above to determine the properties of the neutron star and SN explosion which formed G328.4+0.2 is unable to do so to much better than an order of magnitude, the different combinations values of P_0 , B_{ns} , E_{sn} , and M_{ej} which are allowed predict different physical properties for G328.4+0.2 which are testable with further observations. For example, in the case of $P_0 = 10$ ms, $B_{\text{ns}} = 8 \times 10^{11}$ G, $E_{\text{sn}} = 1 \times 10^{51}$ ergs, and $M_{\text{ej}} = 1 M_{\odot}$, G328.4+0.2 is $\sim 13,000$ years old, twice the age predicted in the ST 2 model as shown in Table 6, and as a result the required velocity of the neutron star is significantly lower, $v_{\text{ns}}^{\text{min}} \sim 500 \text{ km s}^{-1}$. The predicted period for the neutron star in this scenario is also significantly slower than required by the ST 2 scenario, $P \sim 24$ ms, with a value of \dot{E} approximately an order of magnitude lower than that in the ST 2 scenario. The termination shock radius for this set of parameters is $\sim 5''$, considerable smaller than the $\sim 8''$ for the ST 2 scenario and detectable with the

5. CONCLUSIONS

In this paper, we first presented new X-ray (§2.1) and radio (§2.2, 2.3) and observations of Galactic non-thermal radio and X-ray source, G328.4+0.2, from which we infer the current properties and evolutionary history of this source (§3.2). We then presented a simple hydrodynamic model for the evolution of a PWN inside a SNR (§4), which is used to determine which values of E_{sn} , M_{ej} , n , P_0 , and B_{ns} are able to reproduce the properties discussed in §3.2 if G328.4+0.2 was a Composite SNR (§4.1.1) or a PWN (§4.1.2). As a result of this analysis, we determine the G328.4+0.2 is a PWN inside an undetected SNR. Though we are not able to precisely determine the properties of the SN explosion and the neutron star which have created this system, our analysis implies that the neutron star in G328.4+0.2 was born with an initial period $P_0 \lesssim 10$ ms, has a lower than average surface dipole magnetic field strength, and has a higher than average spatial velocity $v_{\text{ns}} \gtrsim 400 \text{ km s}^{-1}$. We assume determining that the SN explosion which created the neutron star had a normal explosion energy, $E_{\text{sn}} \sim 10^{51}$ ergs, but a relative low ejecta mass, $M_{\text{ej}} \lesssim 4M_{\odot}$. Future X-ray and radio observations can significantly decrease this uncertainty, particularly if they are able to either detect pulsations from the neutron star or continuum X-ray or radio emission from the currently undetected SNR in this system.

While we are not able to definitely determine the initial period (P_0) or surface magnetic field strength (B_{ns}) of the neutron star, nor the kinetic energy (E_{sn}) or ejecta mass (M_{ej}) of the progenitor SN explosion, the estimates quoted above are of interest. Our non-detection of the pulsar via radio pulsations is not particularly constraining, due to the very large distance of the PWN. The low

magnetic field but rapid initial period predicted for the neutron star in G328.4+0.2 has implications for models concerning the origin of neutron star magnetic fields. For example, according to the $\alpha - \Omega$ dynamo model of (Thompson & Duncan 1993), neutron star born spinning rapidly ($P_0 \lesssim 5$ ms) should have a strong dipole component to their surface magnetic fields ($B_{\text{ns}} \gg 10^{12}$ G). If the ST 2 scenario proves to be correct, then the low magnetic field of the neutron star in this system would be a problem for such a model. Additionally, the low ejecta mass inferred in this scenario requires that the progenitor of this system was either a single, massive star ($M \gtrsim 35M_{\odot}$) which exploded in a Type Ib/c SN (Woosley et al. 1995), or was initially in a binary system.

Finally, the method used in this paper to study G328.4+0.2 is complementary to other methods used (e.g. Chevalier 2005) to infer the initial period and magnetic field strength of other neutron stars in young PWN as well as the properties of the SN explosion in which they were formed, and is easily applicable to other such systems.

JDG would like to thank Niccolo Bucciantini, Shami Chatterjee, Roger Chevalier, Tracey DeLaney, David Kaplan, Kelly Korreck, Cara Rakowski, and John Raymond for useful discussions, and the anonymous referee for many useful comments. We are extremely grateful to John Reynolds for prompt scheduling and observing assistance at Parkes in 2007. The Australia Telescope is funded by the Commonwealth of Australia for operation as a National Facility managed by CSIRO. JDG and BMG were supported in this work by *XMM* grant NAG5-13202 and LTSA grant NAG5-13032.

REFERENCES

- Aschenbach, B., Egger, R., & Trumper, J. 1995, *Nature*, 373, 587
 Bandiera, R. 1984, *A&A*, 139, 368
 Blondin, J. M., Chevalier, R. A., & Frierson, D. M. 2001, *ApJ*, 563, 806
 Blondin, J. M., Wright, E. B., Borkowski, K. J., & Reynolds, S. P. 1998, *ApJ*, 500, 342
 Bock, D. C.-J., Turtle, A. J., & Green, A. J. 1998, *AJ*, 116, 1886
 Buccieri, R., Bennett, K., Bignami, G. F., Bloemen, J. B. G. M., Boriakoff, V., Caraveo, P. A., Hermsen, W., Kanbach, G., Manchester, R. N., Masnou, J. L., Mayer-Hasselwander, H. A., Ozel, M. E., Paul, J. A., Sacco, B., Scarsi, L., & Strong, A. W. 1983, *A&A*, 128, 245
 Bucciantini, N., Amato, E., Bandiera, R., Blondin, J. M., & Del Zanna, L. 2004, *A&A*, 423, 253
 Bucciantini, N., Blondin, J. M., Del Zanna, L., & Amato, E. 2003, *A&A*, 405, 617
 Camilo, F., Manchester, R. N., Gaensler, B. M., & Lorimer, D. R. 2002a, *ApJ*, 579, L25
 Camilo, F., Manchester, R. N., Gaensler, B. M., Lorimer, D. R., & Sarkissian, J. 2002b, *ApJ*, 567, L71
 Camilo, F., Ransom, S. M., Gaensler, B. M., Slane, P. O., Lorimer, D. R., Reynolds, J., Manchester, R. N., & Murray, S. S. 2006, *ApJ*, 637, 456
 Camilo, F., Stairs, I. H., Lorimer, D. R., Backer, D. C., Ransom, S. M., Klein, B., Wielebinski, R., Kramer, M., McLaughlin, M. A., Arzoumanian, Z., & Müller, P. 2002c, *ApJ*, 571, L41
 Cash, W. 1979, *ApJ*, 228, 939
 Chevalier, R. A. 1982, *ApJ*, 258, 790
 —. 1998, *Memorie della Societa Astronomica Italiana*, 69, 977
 —. 2005, *ApJ*, 619, 839
 Chevalier, R. A. & Emmering, R. T. 1989, *ApJ*, 342, L75
 Chevalier, R. A. & Fransson, C. 1992, *ApJ*, 395, 540
 Chevalier, R. A. & Liang, E. P. 1989, *ApJ*, 344, 332
 Cordes, J. M. & Lazio, T. J. W. 2002, *ArXiv Astrophysics e-prints*
 Dickel, J. R., Milne, D. K., & Strom, R. G. 2000, *ApJ*, 543, 840
 Faucher-Giguère, C.-A. & Kaspi, V. M. 2006, *ApJ*, 643, 332
 Freeman, P., Doe, S., & Siemiginowska, A. 2001, in *Proc. SPIE Vol. 4477*, p. 76-87, *Astronomical Data Analysis*, Jean-Luc Starck; Fionn D. Murtagh; Eds., 76-87
 Gaensler, B. M., Dickel, J. R., & Green, A. J. 2000, *ApJ*, 542, 380
 Gaensler, B. M. & Slane, P. O. 2006, *ARA&A*, 44, 17
 Ghizzardi, S. & Molendi, S. 2002, in *Proc. 'New Visions of the X-ray Universe in the XMM-Newton and Chandra Era' 26-30 Nov. 2001 F. Jansen; Eds.*
 Gotthelf, E. V. 2003, *ApJ*, 591, 361
 Goussard, J.-O., Haensel, P., & Zdenek, J. L. 1998, *A&A*, 330, 1005
 Helfand, D. J. & Becker, R. H. 1987, *ApJ*, 314, 203
 Hobbs, G., Lorimer, D. R., Lyne, A. G., & Kramer, M. 2005, *MNRAS*, 360, 974
 Hughes, J. P., Slane, P. O., & Plucinsky, P. P. 2000, *ApJ*, 542, 386
 Johnston, S., McClure-Griffiths, N. M., & Koribalski, B. 2004, *MNRAS*, 348, L19
 Jun, B.-I. 1998, *ApJ*, 499, 282
 Jun, B.-I., Jones, T. W., & Norman, M. L. 1996, *ApJ*, 468, L59+
 Katz-Stone, D. M. & Rudnick, L. 1997, *ApJ*, 488, 146
 Kennel, C. F. & Coroniti, F. V. 1984, *ApJ*, 283, 710
 Leahy, D. A., Elsner, R. F., & Weisskopf, M. C. 1983, *ApJ*, 272, 256
 Lorimer, D. R., Yates, J. A., Lyne, A. G., & Gould, D. M. 1995, *MNRAS*, 273, 411
 Matheson, H. & Safi-Harb, S. 2005, *Advances in Space Research*, 35, 1099
 Mavromatakis, F., Xilouris, E., & Boumis, P. 2004, *A&A*, 426, 567
 McClure-Griffiths, N. M., Dickey, J. M., Gaensler, B. M., Green, A. J., Haverkorn, M., & Strasser, S. 2005, *ApJS*, 158, 178
 Mills, B. Y., Slee, O. B., & Hill, E. R. 1961, *Australian Journal of Physics*, 14, 497
 Possenti, A., Cerutti, R., Colpi, M., & Mereghetti, S. 2002, *A&A*, 387, 993

- Ransom, S. M., Eikenberry, S. S., & Middleditch, J. 2002, *AJ*, 124, 1788
- Reynolds, S. P. 1985, *ApJ*, 291, 152
- Reynolds, S. P. & Chevalier, R. A. 1984, *ApJ*, 278, 630
- Roberts, M. S. E., Tam, C. R., Kaspi, V. M., Lyutikov, M., Vasisht, G., Pivovarov, M., Gotthelf, E. V., & Kawai, N. 2003, *ApJ*, 588, 992
- Shapiro, S. L. & Teukolsky, S. A. 1983, *Black holes, white dwarfs, and neutron stars: The physics of compact objects* (Research supported by the National Science Foundation. New York, Wiley-Interscience, 1983, 663 p.)
- Shull, J. M., Fesen, R. A., & Saken, J. M. 1989, *ApJ*, 346, 860
- Slane, P., Helfand, D. J., van der Swaluw, E., & Murray, S. S. 2004, *ApJ*, 616, 403
- Tam, C., Roberts, M. S. E., & Kaspi, V. M. 2002, *ApJ*, 572, 202
- Thompson, C. & Duncan, R. C. 1993, *ApJ*, 408, 194
- Truelove, J. K. & McKee, C. F. 1999, *ApJS*, 120, 299
- van der Swaluw, E., Achterberg, A., Gallant, Y. A., & Tóth, G. 2001, *A&A*, 380, 309
- van der Swaluw, E., Downes, T. P., & Keegan, R. 2004, *A&A*, 420, 937
- Velazquez, P. F., Gomez, D. O., Dubner, G. M., de Castro, G. G., & Costa, A. 1998, *A&A*, 334, 1060
- Warren, J. S., Hughes, J. P., & Slane, P. O. 2003, *ApJ*, 583, 260
- Woosley, S. E., Langer, N., & Weaver, T. A. 1995, *ApJ*, 448, 315

TABLE 1
SPATIAL COMPONENTS OF THE X-RAY EMISSION FROM G328.4+0.2

COMPONENT	PARAMETER	VALUE
background	constant	$0.09^{+0.06}_{-0.07}$
Clump 1	r_0	$1''.1^{+1''.5}_{-0''.7}$
	Position	$15^{\text{h}}55^{\text{m}}26^{\text{s}}.68^{+0^{\text{s}}.04}_{-0^{\text{s}}.05}, -53^{\circ}18'02''.7^{+0''.6}_{-0''.6}$
	A	$6.6^{+27.6}_{-3.2}$
	α	$0.9^{+1.0}_{-0.3}$
Clump 2	FWHM	$19''^{+10''}_{-10''}$
	Position	$15^{\text{h}}55^{\text{m}}27^{\text{s}}.5^{+0^{\text{s}}.2}_{-0^{\text{s}}.1}, -53^{\circ}17'54''.6^{+3''.4}_{-3''.8}$
	e	$0.4^{+0.2}_{-0.3}$
	θ	$280^{\circ+20^{\circ}}_{-80^{\circ}}$
	A	$0.8^{+0.3}_{-0.2}$
Diffuse	FWHM	67^{+18}_{-11}
	Position	$15^{\text{h}}55^{\text{m}}26^{\text{s}}.6^{+0^{\text{s}}.2}_{-0^{\text{s}}.2}, -53^{\circ}17'48''.3^{+5''}_{-4''}$
	e	$0.4^{+0.1}_{-0.1}$
	θ	$130^{\circ+10^{\circ}}_{-10^{\circ}}$
	A	$0.4^{+0.1}_{-0.1}$

NOTE. – Results from the spatial fit to the X-ray emission from G328.4+0.2, as described in §2.1.1. Fitting was done using the SHERPA software package, and the errors reflect the 90% confidence level. Clump 1 was fitted to a 2D Lorentzian, defined as $f(r) = A \left(1 + \frac{r^2}{r_0^2}\right)^{-\alpha}$, where $f(r)$ is the expected number of counts at radius r away from the center of the source, A is given in counts, and the core-radius r_0 is in arc-seconds. The background component is given in counts pixel $^{-1}$. Both Clump 2 and Diffuse were modeled with elliptical 2D Gaussians, where the full width, half maximum (FWHM) is given in arc-seconds, the ellipticity is e , defined as $1 - b/a$, where b and a are, respectively, the major and minor axis of the source, the position angle θ is given in degrees counterclockwise from north, and the amplitude A is given in counts.

TABLE 2
SPECTRAL FITS TO MOS1 + MOS2 + PN DATA

PARAMETER	Value			
Model	phabs * pow	phabs * bbodyrad	phabs * brems	phabs * ray
N_H	$11.6^{+3}_{-2} \times 10^{22}$	$6.4^{+1}_{-1} \times 10^{22}$	$10.4^{+2}_{-1} \times 10^{22}$	$7.8^{+1}_{-1} \times 10^{22}$
Γ or kT	$2.0^{+0.4}_{-0.2}$	$1.6^{+0.1}_{-0.1}$	9.5^{+5}_{-3}	$62.9^{+>900}_{-30}$
Absorbed Flux	$4.6^{+1}_{-3} \times 10^{-13}$	$4.4^{+0.1}_{-0.5} \times 10^{-13}$	$4.5^{+0.4}_{-1.5} \times 10^{-13}$	$4.9^{+0.3}_{-2.6} \times 10^{-13}$
Unabsorbed Flux	$1.9^{+0.1}_{-0.9} \times 10^{-12}$	$6.5^{+0.1}_{-1.0} \times 10^{-13}$	$1.2^{+0.1}_{-0.5} \times 10^{-12}$	$9.6^{+0.1}_{-4.2} \times 10^{-13}$
χ^2	103.3/131	98.4/131	101.7/131	122.8/131
Reduced χ^2	0.81/128	0.77/128	0.79/128	0.96/128

NOTE – Results from joint fits to the MOS1, MOS2, and PN spectrum between 0.5 and 10 keV. The model **phabs * pow** refers to a power-law attenuated by interstellar absorption, **phabs * bbodyrad** refers to a blackbody attenuated by interstellar absorption, **phabs * brems** refers to a Bremsstrahlung source spectrum attenuated by interstellar absorption, and **phabs * ray** refers to a Raymond-Smith thermal plasma spectrum attenuated by interstellar absorption. In the table, N_H is given in cm $^{-2}$, kT in keV, and flux in ergs cm $^{-2}$ s $^{-1}$, both the absorbed and unabsorbed flux are calculated between 0.5 and 10 keV, and the errors represent the 90% confidence level.

TABLE 3
EXPECTED PROPERTIES OF G328.4+0.2 IF IT IS A COMPOSITE SNR

<i>Supernova Remnant Properties</i>		<i>Pulsar Wind Nebula Properties</i>		<i>Neutron Star Properties</i>	
PARAMETER	VALUE	PARAMETER	VALUE	PARAMETER	VALUE
E_{sn}	1×10^{51} ergs	E_{pwn}	4.8×10^{50} ergs	\dot{E}_0	2.5×10^{40} ergs s $^{-1}$
M_{ej}	$1 M_{\odot}$	R_{pwn}	8.7 parsecs	P_0	3.8 ms
Phase	Sedov-Taylor	$M_{\text{sw}}^{\text{pwn}}$	$5.3 M_{\odot}$	τ_0	1730 years
$P_{\text{snr}}(R_{\text{pwn}})$	1.4×10^{-9} dynes	P_{pwn}	2.0×10^{-9} erg cm $^{-4}$	B_{ns}	1.1×10^{12} G
$v_{\text{ej}}(R_{\text{pwn}})$	400 km s $^{-1}$	v_{pwn}	700 km s $^{-1}$	$v_{\text{ns}}^{\text{min}}$	1300 km s $^{-1}$
t_{now}	4900 years	r_{ts}	0.5 parsecs	\dot{E}	1.7×10^{39} ergs s$^{-1}$
n	0.32 cm^{-3}	θ_{ts}	6''7	P	7.5 ms
...	\dot{P}	1.8×10^{-14} s/s
...	τ_c	6700 years
...	E_{psr}	1.0×10^{51} ergs

NOTE. – The values in **bold** are model assumptions, while the others are predicted by the model presented in §4. $P_{\text{snr}}(R_{\text{pwn}})$ is the pressure inside of the SNR just outside of the PWN, $v_{\text{ej}}(R_{\text{pwn}})$ is the velocity of material inside the SNR just outside of the PWN, E_{pwn} is the internal energy of the PWN, R_{pwn} is the radius of the PWN, $M_{\text{sw}}^{\text{pwn}}$ is the mass of material swept up by the PWN, P_{pwn} is the internal pressure of the PWN, v_{pwn} is the expansion velocity of the PWN, r_{ts} is the radius of the termination shock around the neutron star inside the PWN, calculated using Equation 16, θ_{ts} is the angular size of this feature assuming $d_{17} \equiv 1$, B_{ns} is the dipole magnetic field of the neutron star in G328.4+0.2 according to this model, P is the period of the neutron star in G328.4+0.2, \dot{P} is the period-derivative of the neutron star, τ_c is the characteristic age of the neutron star, defined as $\tau_c = P/(2\dot{P})$, and E_{psr} is the total amount of energy injected by the neutron star into G328.4+0.2 for $t < t_{\text{now}}$. All values are given for $t = t_{\text{now}}$ unless otherwise noted.

TABLE 4
SCENARIOS FOR G328 AS A PWN INSIDE AN UNDETECTED SNR

Scenario #	τ_0	P_0	$E_{\text{sn},51}$	M_{ej}	n	t_{now}	SNR Phase	R_{snr}	$B_{\text{ns},12}$	$v_{\text{ns}}^{\text{min}}$	$v_{\text{ns}}^{\text{min},\text{II}}$
ST 1	1730	5.0	1.00	1	0.03	5100	Sedov-Taylor	19.8	0.5	1300	2400
ST 2	1730	5.0	3.16	1	0.03	6500	Sedov-Taylor	28.0	0.5	1000	1900
Rad 1	430	10.0	0.32	10	0.32	84200	Radiative	28.4	2.0	100	100
Rad 2	770	10.0	0.32	10	0.32	52400	Radiative	24.8	1.5	100	200
Rad 3	770	10.0	0.32	10	1.00	101400	Radiative	22.1	1.5	100	100

NOTE. – Values for τ_0 , P_0 , E_{sn} , M_{ej} , and n that satisfy the criteria listed in §4.1.2 for G328 being a PWN inside an undetected SNR. The value of τ_0 is given in years, P_0 in ms, $E_{\text{sn},51} \equiv E_{\text{sn}}/10^{51}$ ergs, M_{ej} in solar masses, n in cm $^{-3}$, t_{now} in years, R_{snr} in parsecs, $B_{\text{ns}} = B_{\text{ns},12} \times 10^{12}$ G, $v_{\text{ns}}^{\text{min}}$ is in km s $^{-1}$, and $v_{\text{ns}}^{\text{min},\text{II}}$ is also in km s $^{-1}$.

TABLE 5
COMPRESSION/EXPANSION PROPERTIES OF G328.4+0.2 IF IT IS A PWN

Scenario #	$t(v_{\text{pwn}} = 0)$	Central Bar Lifetime	$R_{\text{pwn}}(v_{\text{pwn}} = 0)$	$\frac{V_{\text{pwn}}^{\text{re-exp}}}{V_{\text{pwn}}^{\text{compres}}}$
ST 1	1648.5, 2432.0	63930	8.20, 7.96	0.91
ST 2	969.0, 1837.0	35250	8.36, 6.34	0.44
Rad 1	12772.0, 26541.0	243480	8.53, 7.55	0.69
Rad 2	13336.5, 21112.5	256230	8.48, 8.27	0.93
Rad 3	9761.5, 11035.0	102640	5.72, 5.72	1.00

NOTE. – In this table, values Scenario # correspond to the values of τ_0 , P_0 , E_{sn} , M_{ej} , and n given in Table 4. $t(v_{\text{pwn}} = 0)$ and the Central Bar lifetime are given in years, and $R_{\text{pwn}}(v_{\text{pwn}} = 0)$ is given in parsecs. $\frac{V_{\text{pwn}}^{\text{re-exp}}}{V_{\text{pwn}}^{\text{compres}}}$ is the ratio of the volume of the PWN at re-expansion and compression.

TABLE 6
EXPECTED PROPERTIES OF G328.4+0.2 IF IT IS A PWN (ST 2 SCENARIO IN TABLE 4)

<i>Supernova Remnant Properties</i>		<i>Pulsar Wind Nebula Properties</i>		<i>Neutron Star Properties</i>	
PARAMETER	VALUE	PARAMETER	VALUE	PARAMETER	VALUE
E_{sn}	3.2×10^{51} ergs	E_{pwn}	3.2×10^{50} ergs	\dot{E}_0	1.5×10^{40} ergs s $^{-1}$
M_{ej}	$1 M_{\odot}$	R_{pwn}	12.5 parsecs	P_0	5 ms
Phase	Sedov-Taylor	$M_{\text{sw}}^{\text{pwn}}$	$0.4 M_{\odot}$	τ_0	1730 years
$P_{\text{snr}}(R_{\text{pwn}})$	3.6×10^{-10} dynes	P_{pwn}	4.4×10^{-10} dynes	B_{ns}	5×10^{11} G
$v_{\text{ej}}(R_{\text{pwn}})$	460 km s $^{-1}$	v_{pwn}	790 km s $^{-1}$	$v_{\text{ns}}^{\text{min}}$	990 km s $^{-1}$
Age (t_{now})	6500 years	r_{ts}	0.6 parsecs	E	6.4×10^{38} ergs s $^{-1}$
n	0.03 cm^{-3}	θ_{ts}	$7''.7$	P	10.9 ms
...	\dot{P}	2.1×10^{-14} s/s
...	τ_c	8200 years
...	E_{psr}	6.3×10^{50} ergs

NOTE. – The model assumptions are given in **bold**. $P_{\text{snr}}(R_{\text{pwn}})$ is the pressure inside just outside of the PWN, $v_{\text{ej}}(R_{\text{pwn}})$ is the velocity of material inside just outside of the PWN, E_{pwn} is the internal energy of the PWN, R_{pwn} is the radius of the PWN, $M_{\text{sw}}^{\text{pwn}}$ is the mass of material swept up by the PWN, P_{pwn} is the internal pressure of the PWN, v_{pwn} is the expansion velocity of the PWN, r_{ts} is the radius of the termination shock around the neutron star inside the PWN, θ_{ts} is the predicated angular radius of this feature assuming $d_{17} \equiv 1$, B_{ns} is the predicted dipole magnetic field of the neutron star in G328.4+0.2, P is the predicted period of the neutron star in G328.4+0.2, \dot{P} is the predicted period-derivative of the neutron star, τ_c is characteristic age of the neutron star, and E_{psr} is the total amount of energy injected by the neutron star into G328.4+0.2 for $t < t_{\text{now}}$. All values are given for $t = t_{\text{now}}$ unless otherwise noted.

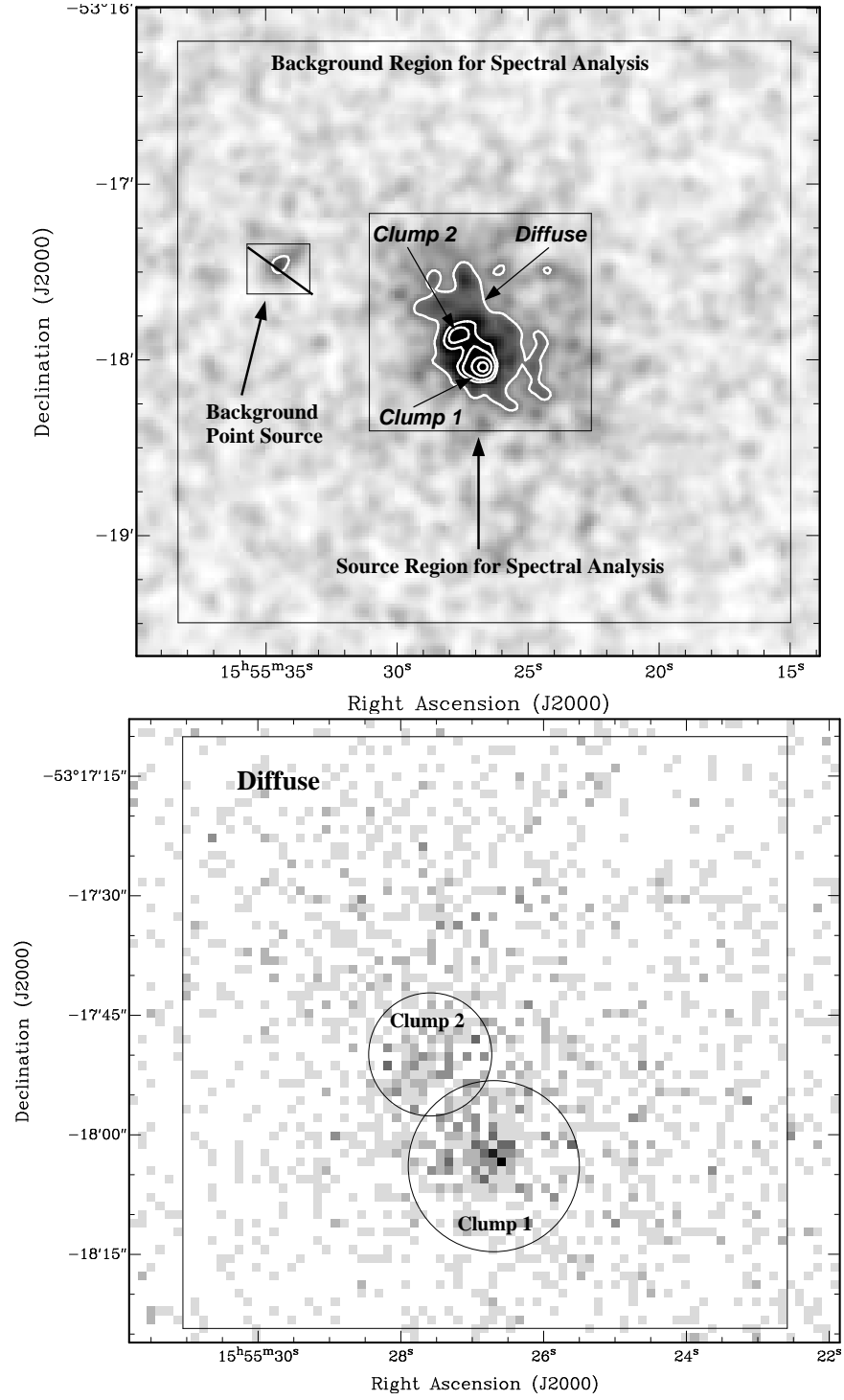


FIG. 1.— *Top*: Exposure normalized, vignette corrected MOS1 + MOS2 image of G328.4+0.2 smoothed by a $5''$ Gaussian. The white contours indicate 20, 40, 50, 70, and 90% of the peak X-ray flux in the smoothed image, while the boxes indicate the background and source regions used for the spectral analysis described in §2.1.2. The background point source labeled in the image was excluded from the background region. Additionally, the labels in this plot point to the morphological features discussed in §2.1.1. *Bottom*: Unsmoothed normalized, vignette corrected MOS1 and MOS2 image of G328.4+0.2 overlaid with the regions used for the Hardness Ratio analysis discussed in §2.1.2.

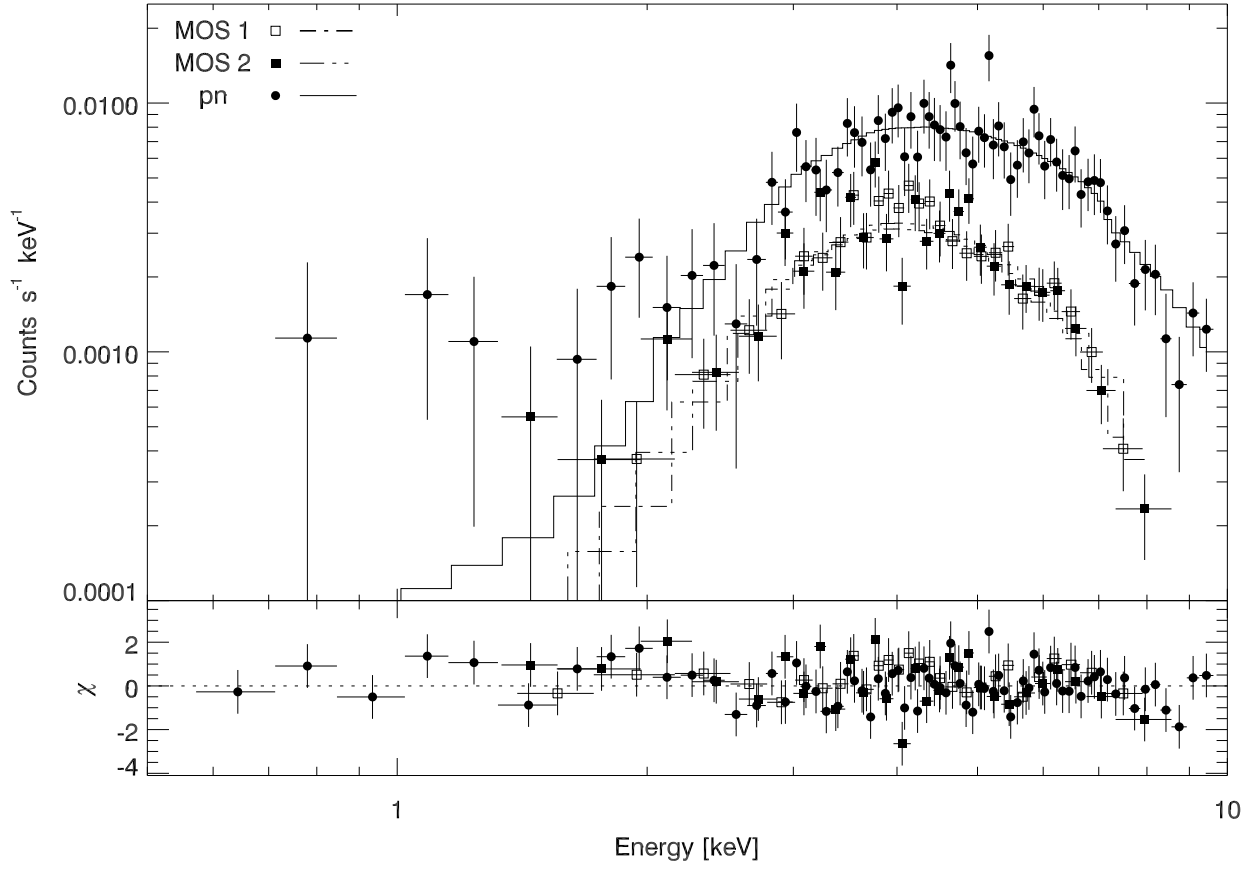


FIG. 2.— Mos1, Mos2, and pn spectrum of G328.4+0.2 overlaid with the absorbed power-law model whose parameters are given in Table 2.

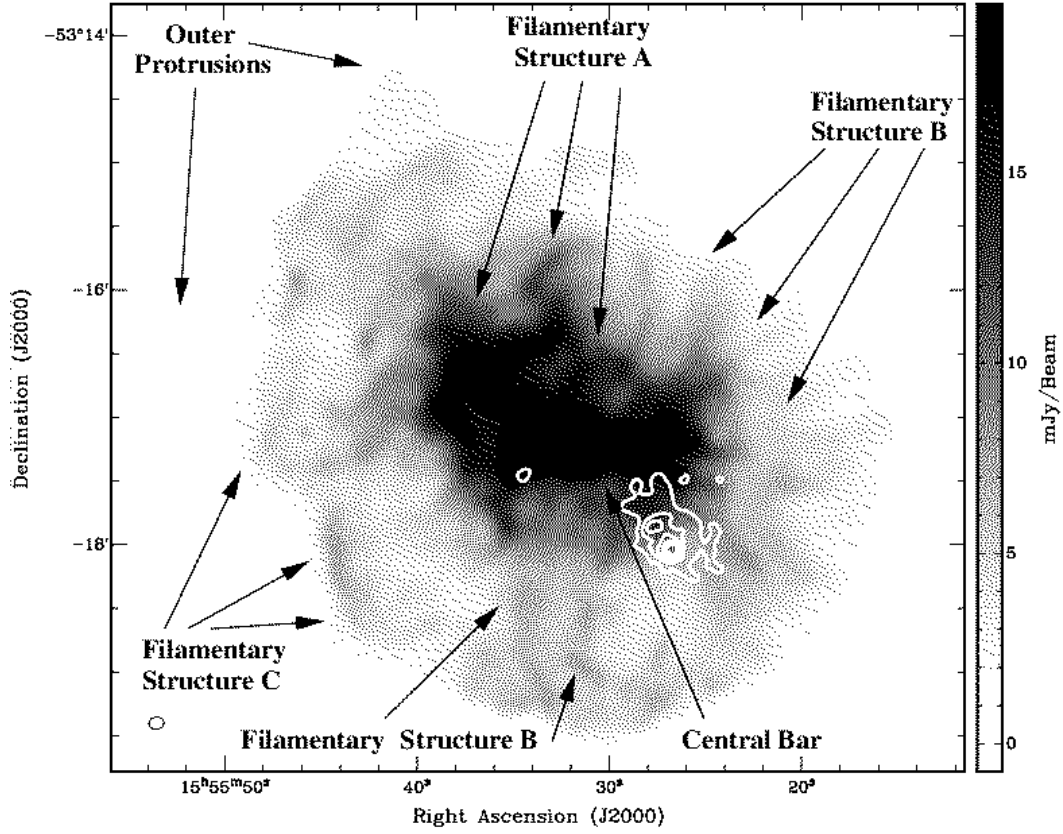


FIG. 3.— 1.4 GHz image of G328.4+0.2, overlaid with X-ray contours in green which represent 20%, 35%, ..., 90% of the peak flux in the smooth X-ray image shown in Fig. 1. The beam size of this image is $7''.0 \times 5''.8$, and is shown in the lower left-hand corner of the image. The labels indicate examples of the different radio morphological features discussed in §2.2.

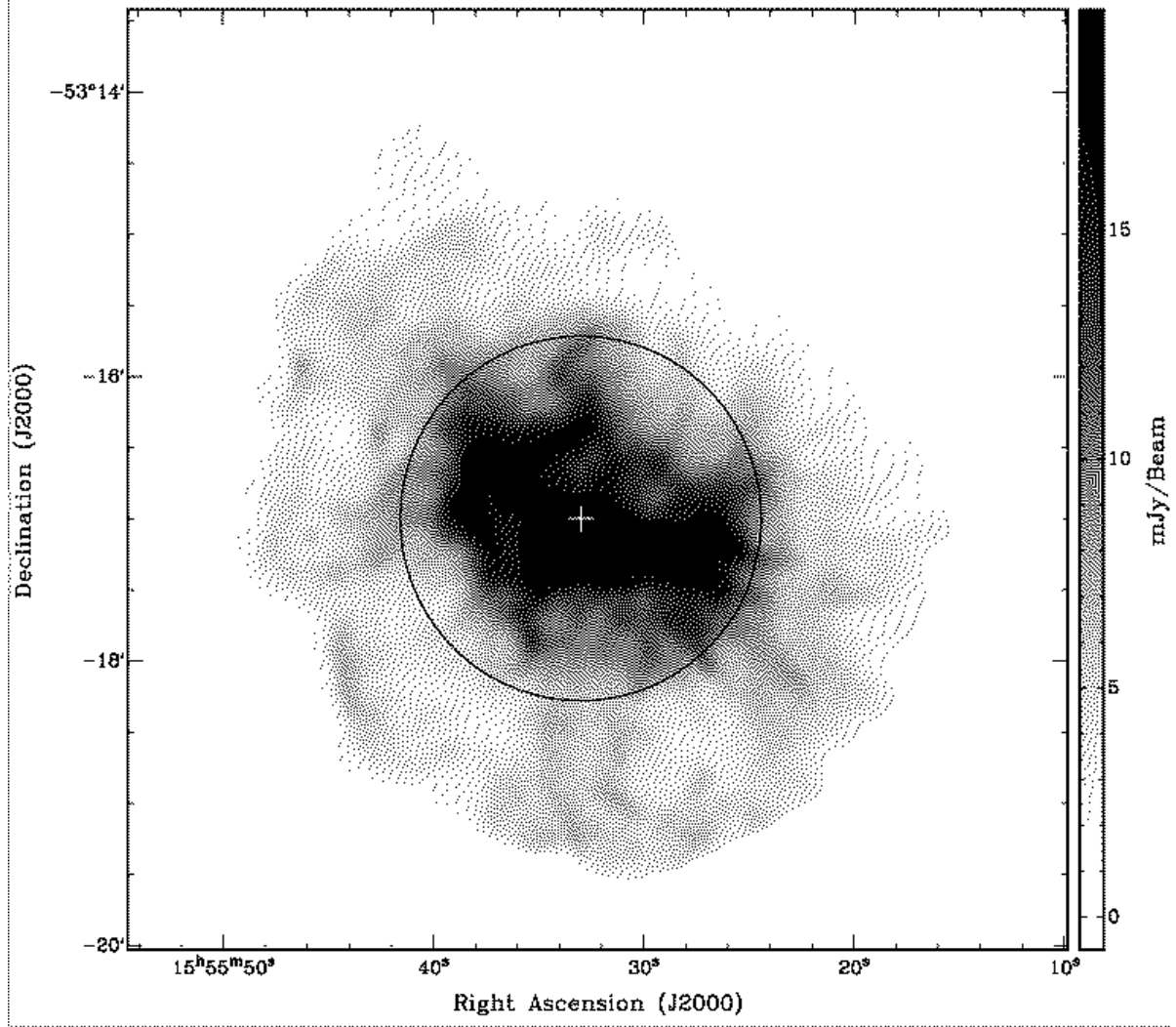


FIG. 4.— 20cm radio image of G328.4+0.2 (same data as shown in Fig. 3), with a color scale chosen to enhance the visibility of Filamentary Structure B discussed in §2.2. The yellow circle indicates the size of PWN predicted in the ST 2 model listed in Table 5 when it re-expanded after the initial compression by the SNR reverse shock, and the white cross indicates the center of G328.4+0.2 ($15^{\text{h}}55^{\text{m}}33^{\text{s}}$, $-53^{\circ}17'00''$; J2000) as determined by Gaensler et al. (2000).

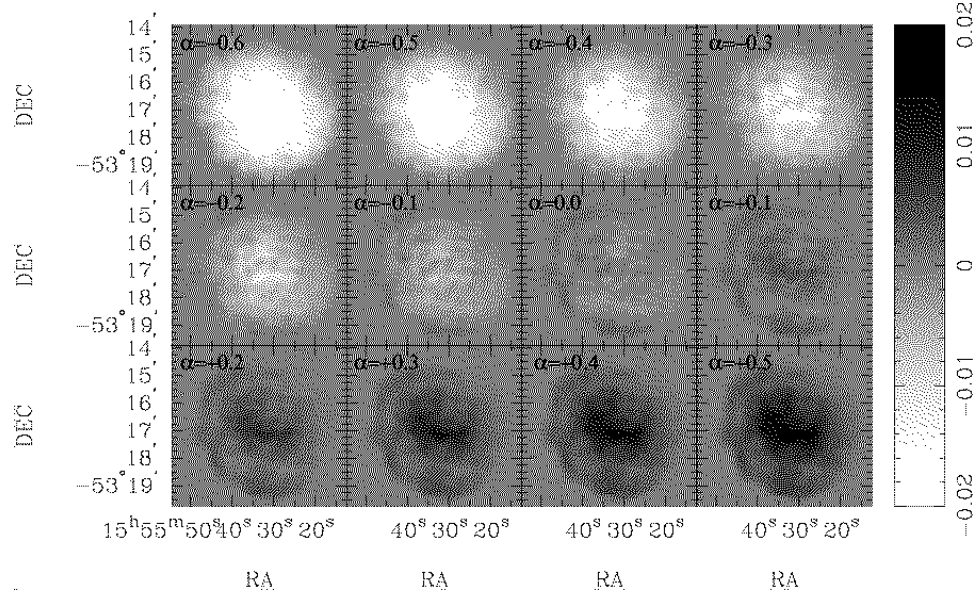


FIG. 5.— Spectral tomography images of G328.4+0.2, as described in §2.2.1. The spectral index α is given in the upper left hand corner of each image, where $S_\nu \propto \nu^\alpha$.

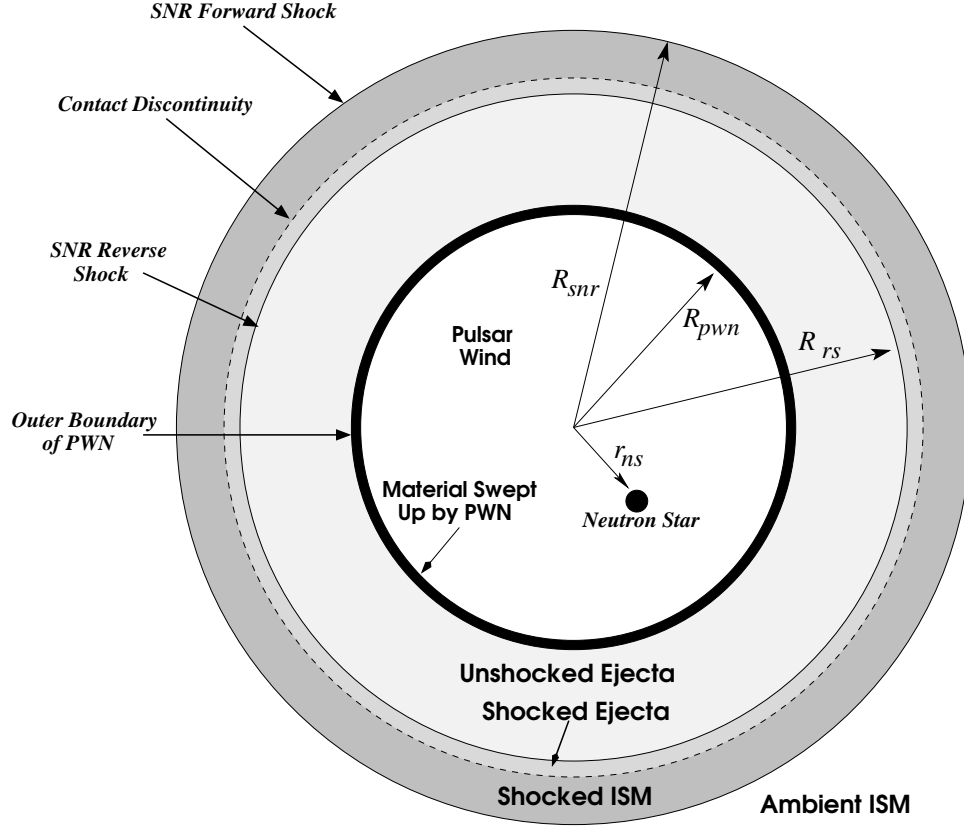


FIG. 6.— Diagram of a Composite SNR in the Free Expansion stage of its evolution. In this image, the ratio between the thickness of the mass shell surrounding the PWN and the radius of the PWN is $1/24$, as determined by van der Swaluw et al. (2001), and the radius of the SNR Forward Shock, Contact Discontinuity, and Reverse Shock radii are equal to the values given in Chevalier (1982) for his $n = 9, s = 0$ case. The colors denote the nature of the material within each region.

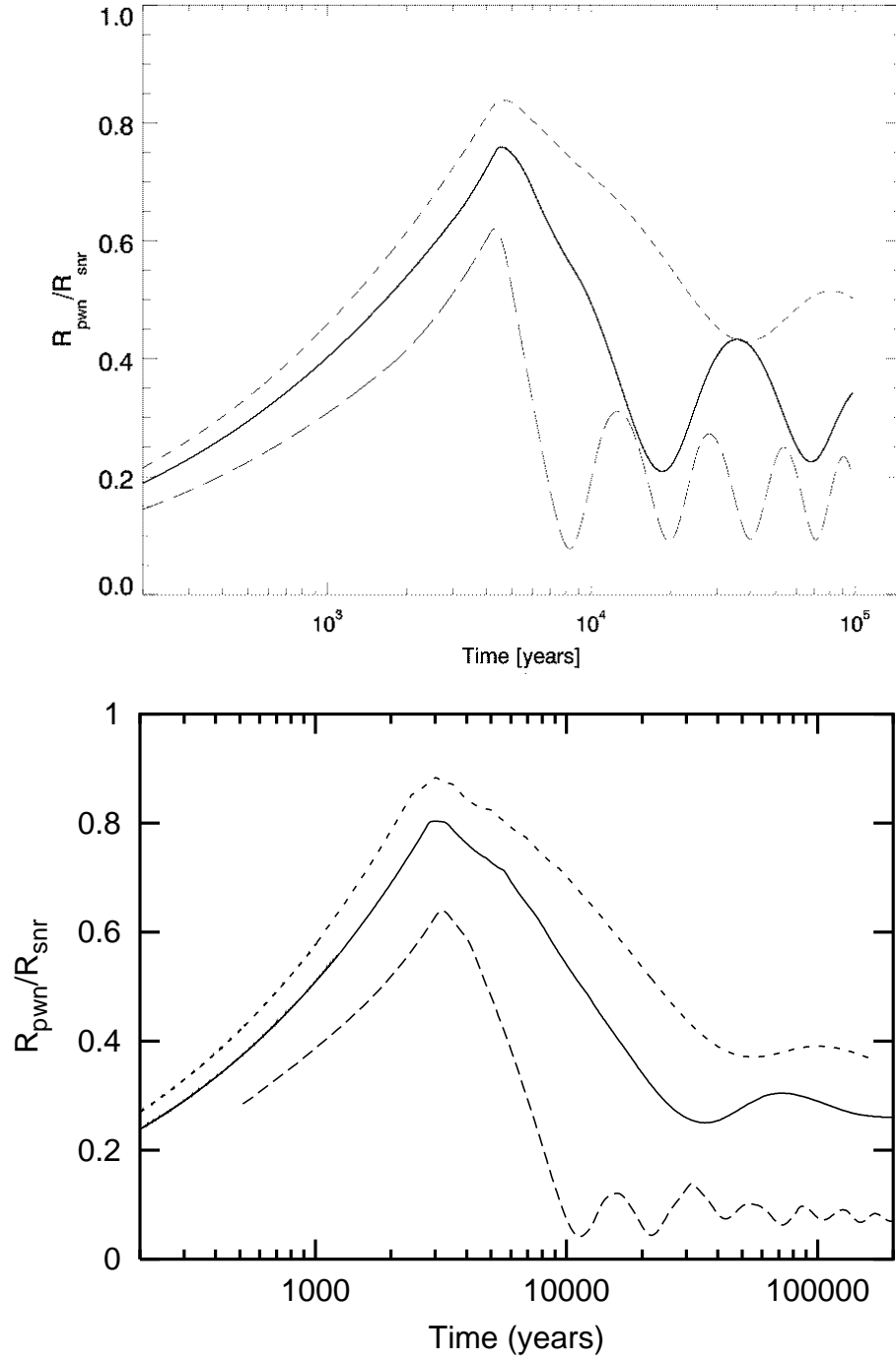


FIG. 7.— $R_{\text{pwn}}/R_{\text{snr}}$ for Models A (*solid*), B (*long-dashed line*), & C (*short-dashed line*) in Blondin et al. (2001). The *top* plot shows the result of the model presented in §4, while the bottom is a reproduction of Fig. 3 by Blondin et al. (2001), reproduced by permission of the AAS.

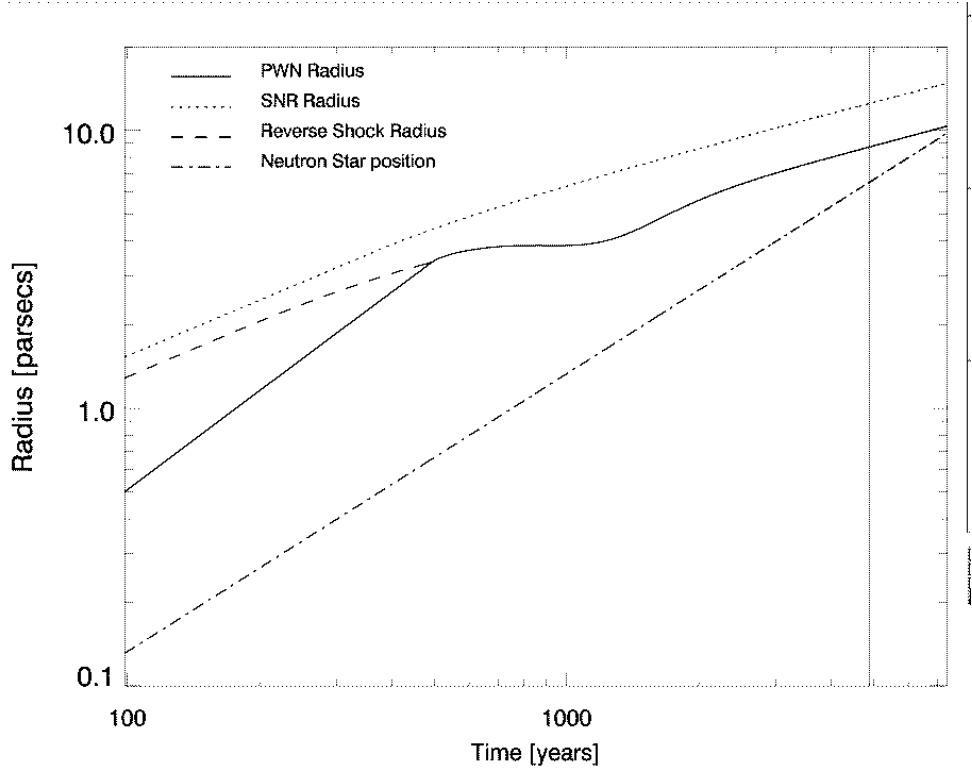


FIG. 8.— The radius of the PWN, SNR, and SNR reverse shock as well as the location of the neutron star as a function of time if G328.4+0.2 is a composite SNR. The vertical line indicates the current age of the system, and the properties of this system are given in Table 3.

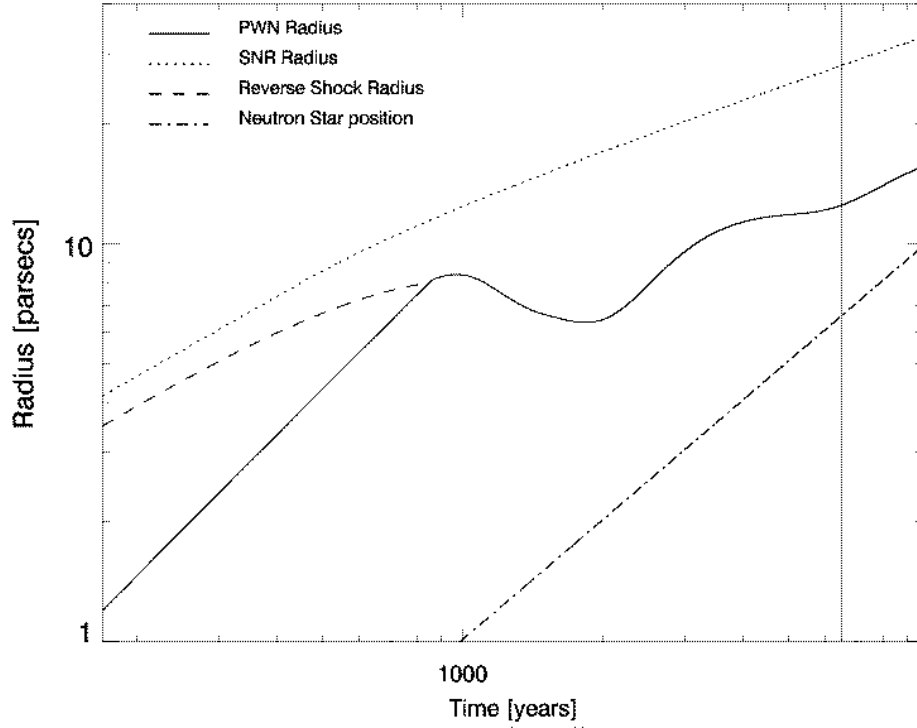


FIG. 9.— The radius of the PWN, SNR, and SNR reverse shock as well as the location of the neutron star as a function of time for the favored (ST 2; Table 4) scenario if G328.4+0.2 is a PWN. The vertical line indicates the current age of the system.

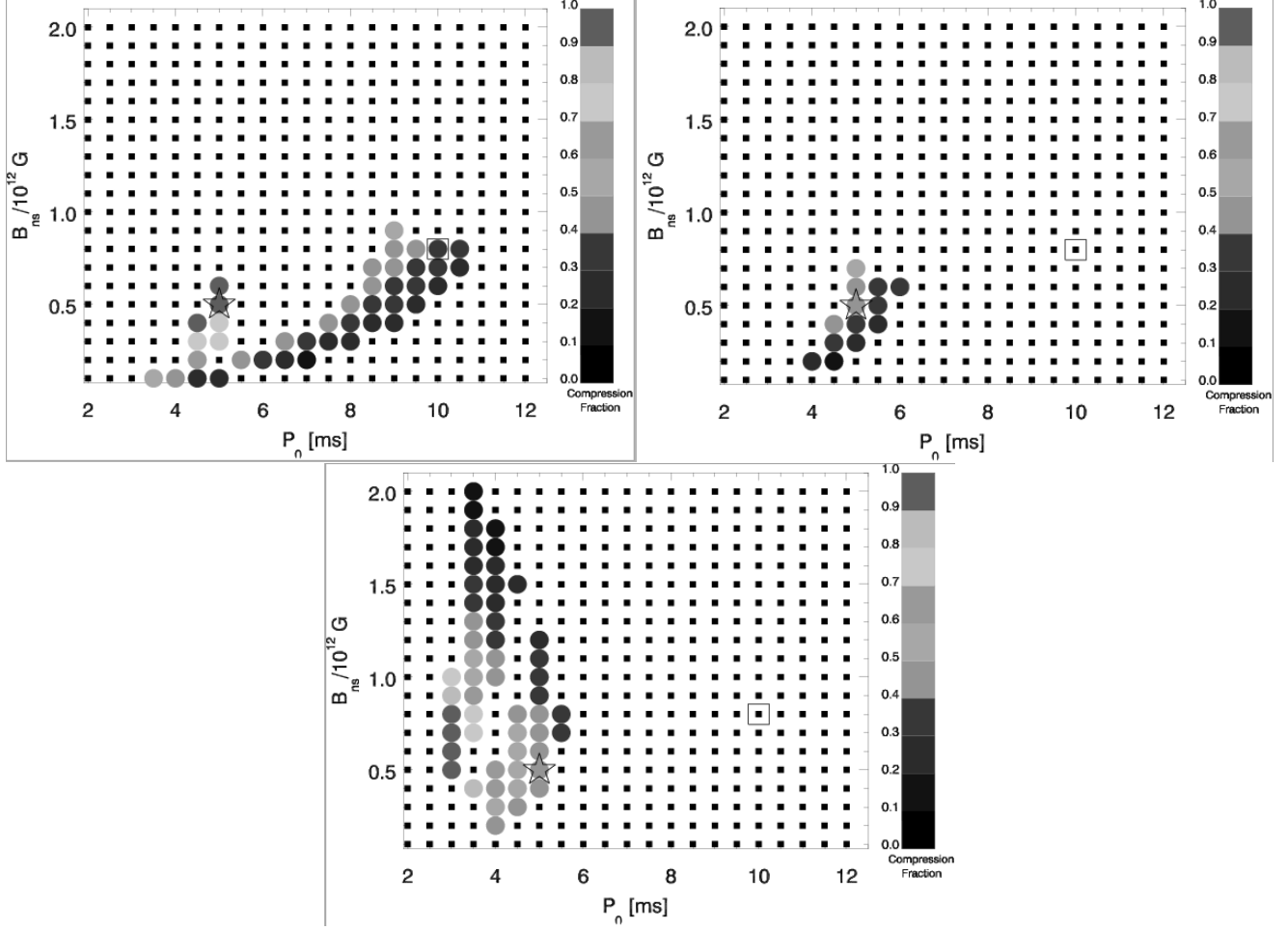


FIG. 10.— The results for varying P_0 and B_{ns} for a $E_{\text{sn}} = 10^{51}$ ergs, $M_{\text{ej}} = 1M_{\odot}$ (*top*), $E_{\text{sn}} = 3 \times 10^{51}$ ergs, $M_{\text{ej}} = 1M_{\odot}$ (*middle*), and $E_{\text{sn}} = 4 \times 10^{51}$ ergs, $M_{\text{ej}} = 3.25M_{\odot}$ (*bottom*) SN explosion, assuming $n = 0.03 \text{ cm}^{-3}$. The small black squares indicate models which failed the criteria described in §4.1.2, while the colored circles indicate scenarios which passed. The color represents the Compression Fraction of the PWN, defined as the ratio of the PWN's volume at the beginning and end of the compression stage. The Compression Fraction of the ST 2 case given in Table 4 is 0.44 (light blue on this color scale), and lower values correspond to a more substantial compression. The star indicates the position of a $P_0 = 5 \text{ ms}$, $B_{\text{ns}} = 5 \times 10^{11} \text{ G}$ neutron star, while the large square indicates the position of a $P_0 = 10 \text{ ms}$, $B_{\text{ns}} = 8 \times 10^{11} \text{ G}$ neutron star – the two neutron stars used in Fig. 11.

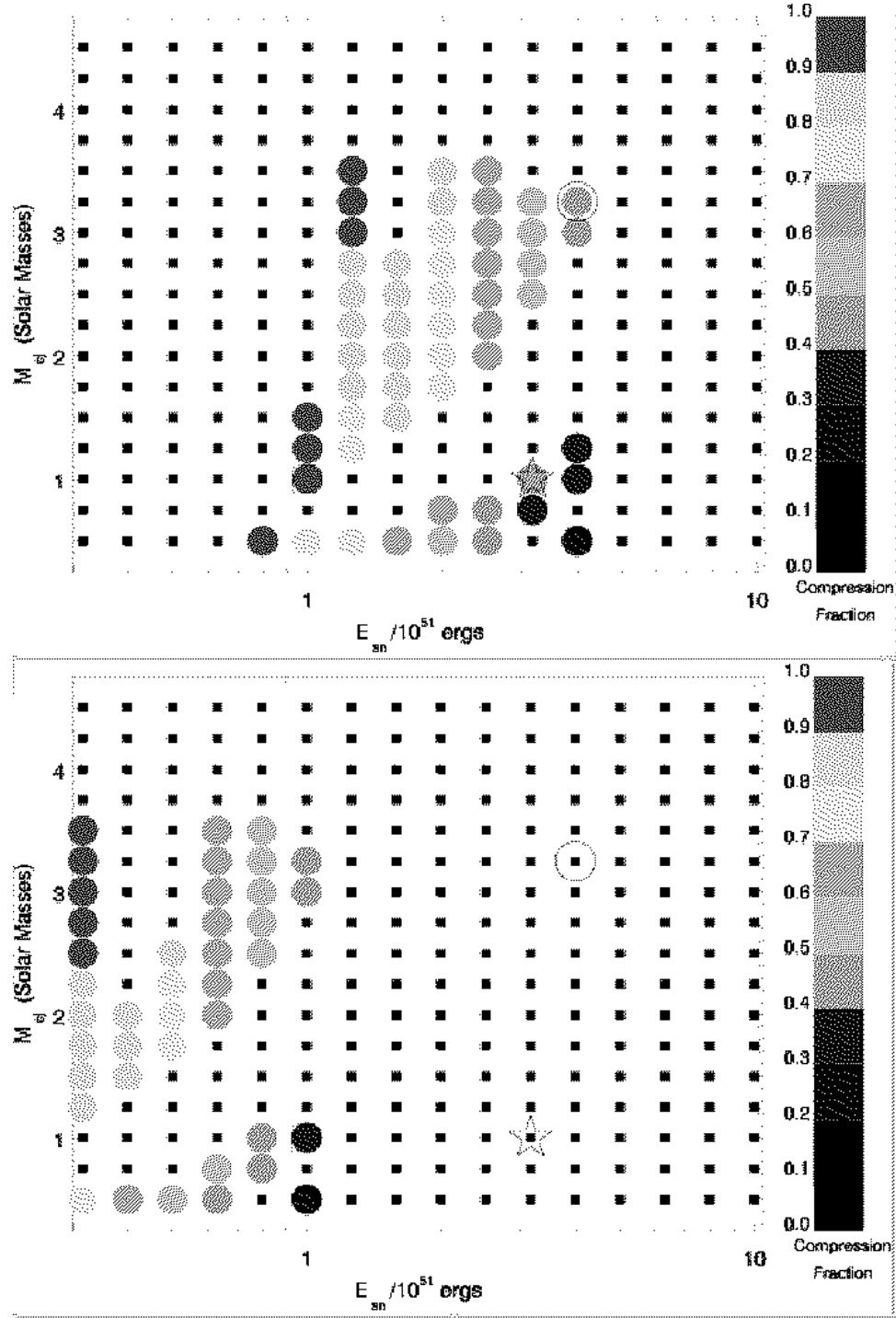


FIG. 11.— The results of varying E_{sn} and M_{ej} for a $P_0 = 5$ ms, $B_{ns} = 5 \times 10^{11}$ G (*top*) and $P_0 = 10$ ms, $B_{ns} = 8 \times 10^{11}$ G (*bottom*) neutron star, assuming $n = 0.03 \text{ cm}^{-3}$. The black squares indicate which scenarios failed the criteria described in §4.1.2, while the colored circles indicate those that passed, with the color representing the Compression Fraction (defined as the ratio of the PWN's volume at the beginning and end of the compression stage) of the PWN. The star indicates a $E_{sn} = 1 \times 10^{51}$ ergs, $M_{ej} = 1 M_{\odot}$ SN explosion, the square indicates a $E_{sn} = 3 \times 10^{51}$ ergs, $M_{ej} = 1 M_{\odot}$ SN explosion, and the circle indicates a $E_{sn} = 4 \times 10^{51}$ ergs, $M_{ej} = 3.25 M_{\odot}$ SN explosion – the SN explosion parameters used in Fig. 10.

APPENDIX

EQUATIONS FOR THE HD MODEL FOR THE EVOLUTION OF A PWN INSIDE A SNR

In this Appendix, we provide many of the details concerning the properties of the neutron star, PWN, and SNR needed to simulate the HD model for the evolution of a PWN inside a SNR described in §4.

For the SNR, we assume that the initial ejecta density profile consists of a constant density core surrounded by a $\rho \propto r^{-9}$ envelope – the standard assumption for a SNR produced by a Type-II SNR (Blondin et al. 2001; Chevalier 1982) – and that the ejecta is expanding ballistically ($v_{\text{ej}} \equiv r_{\text{ej}}/t$). The boundary between the constant density core and the outer ejecta envelope has a velocity v_{core} , defined as (Blondin et al. 2001):

$$v_{\text{core}} = \left(\frac{20}{9} \frac{E_{\text{sn}}}{M_{\text{ej}}} \right)^{1/2} \quad (\text{A1})$$

where E_{sn} is the explosion energy of the SN and M_{ej} is the ejecta mass. As a result, the density ρ_{core} of the ejecta core is (Blondin et al. 2001):

$$\rho_{\text{core}}(t) = \frac{10}{9\pi} E_{\text{sn}} v_{\text{core}}^{-5} t^{-3}. \quad (\text{A2})$$

As the SNR expands, it sweeps up and shocks the surrounding interstellar medium (ISM). This swept-up material has a higher pressure than the cold ejecta driving the expansion of the SNR, and as a result drives a reverse shock (RS) into the SN ejecta. In between the outer edge of the SNR, which marks the location of the forward shock (FS) and the RS is a contact discontinuity which separates the shocked ISM from the ejecta shocked by the RS. The pressure inside the SNR at $r < r_{\text{rs}}$, where r_{rs} is the radius of the RS, is assumed to be zero. A diagram of this is shown in Fig. 6. Since we assume that both the SN ejecta and the shocked ISM behave as a $\gamma = 5/3$ perfect gas, the sound speed c_s of this material is:

$$c_s \equiv \sqrt{\frac{5}{3} \frac{P}{\rho}} \quad (\text{A3})$$

When the RS is still in the ejecta envelope, we determine the pressure, velocity, and density profiles on the material between the RS and FS using the self-similar equations given by Chevalier (1982), evaluating them for the $n = 9$, $s = 0$ case. However, when the RS enters the constant density ejecta core, it is no longer possible to apply the self-similar solution of Chevalier (1982), and we use the work of Truelove & McKee (1999) to determine the radius of the RS and the results given by Bandiera (1984) to determine the pressure, velocity, and density profiles between the RS and FS. It is also necessary to model the radius of the FS (R_{snr}), which we do using the work of Truelove & McKee (1999). This is valid while the SNR is in the Free Expansion and Sedov-Taylor phases of its evolutions. After the SNR goes radiative, which occurs at a time $t = t_{\text{rad}}$ defined as (Blondin et al. 1998):

$$t_{\text{rad}} \approx 2.9 E_{51}^{\frac{4}{17}} n^{-\frac{9}{17}} \times 10^4 \text{ yr}. \quad (\text{A4})$$

After this point, $R_{\text{snr}} \propto t^{2/7}$. An analytic model for the pressure, velocity, and density distribution of a SNR in this phase does not currently exist, and therefore it is difficult to extend our model to this phase, though if one assumes that the interior of the SNR evolves adiabatically, $R_{\text{pwn}}/R_{\text{snr}} \propto t^{0.075}$ for $t > t_{\text{rad}}$ (Blondin et al. 2001).

For the PWN, as mentioned in §4, we assume that it is a bubble filled with a $\gamma = 4/3$ perfect gas. As a result, the internal pressure of the PWN, P_{pwn} is equal to:

$$P_{\text{pwn}} = \frac{E_{\text{pwn}}}{3V_{\text{pwn}}}, \quad (\text{A5})$$

where E_{pwn} is the internal energy of the PWN and V_{pwn} is the volume of the PWN, defined as:

$$V_{\text{pwn}} = \frac{4}{3} \pi R_{\text{pwn}}^3 \quad (\text{A6})$$

where R_{pwn} is the radius of the PWN. The internal energy of the PWN is determined by the rate of energy injected into the PWN by the neutron star (\dot{E}), and energy loss due to its expansion inside the SNR ($E_{\text{pwn}}^{\text{ad}}$). For \dot{E} , we use the standard assumption that it is equal to:

$$\dot{E} = \dot{E}_0 \left(1 + \frac{t}{\tau_0} \right)^{-\frac{p+1}{p-1}} \quad (\text{A7})$$

where t is the age of the neutron star, p is the pulsar braking index ($p = 3$ for a magnetic dipole), τ_0 is the characteristic timescale of pulsar spin-down, and \dot{E}_0 is the initial spin-down energy of the neutron star. Both τ_0 and \dot{E}_0 depend on the physical properties of the neutron star, with τ_0 defined as (Blondin et al. 2001; Shapiro & Teukolsky 1983):

$$\tau_0 = \frac{3c^3 I P_0^2}{4\pi^2 B_{\text{ns}}^2 R_{\text{ns}}^6 \sin^2 \alpha} \quad (\text{A8})$$

where I is the neutron star's moment of inertia, P_0 is the initial spin period, B_{ns} is the magnetic field of the neutron star, R_{ns} is the radius of the neutron star, α is the angle between the neutron star's rotation axis and magnetic field, and (Blondin et al. 2001):

$$\dot{E}_0 = I \left(\frac{2\pi}{P_0} \right)^2 \frac{1}{\tau_0(p-1)}. \quad (\text{A9})$$

Since the PWN expands adiabatically, $\dot{E}_{\text{pwn}}^{\text{ad}}$ is equal to:

$$\dot{E}_{\text{pwn}}^{\text{ad}} = -\frac{E_{\text{pwn}}}{t}. \quad (\text{A10})$$

As a result, the change in the internal energy of the PWN over time (\dot{E}_{pwn}) is equal to:

$$\dot{E}_{\text{pwn}} = -\frac{E_{\text{pwn}}}{t} + \dot{E}_0 \left(1 + \frac{t}{\tau_0} \right)^{-2} \quad (\text{A11})$$

assuming that $p = 3$. This equation can be solved analytical, and we result that $E_{\text{pwn}}(t)$ can be expressed as:

$$E_{\text{pwn}}(t) = \dot{E}_0 \tau_0 \left(\frac{\ln(1 + t/\tau_0)}{t/\tau_0} - \frac{1}{t/\tau_0 - 1} \right). \quad (\text{A12})$$

When we run our model, we use Eq. (A12) to determine the initial value of E_{pwn} , but determine E_{pwn} at later times using the procedure described in Step 2 in §4.

During its free-expansion, the PWN is moving faster than its surroundings, and the mass of the shell surrounding the PWN ($M_{\text{sw,pwn}}$) is simply:

$$M_{\text{sw,pwn}}(t) = \int_0^{R_{\text{pwn}}} 4\pi R^2 \rho_{\text{ej}}(r, t) dr \quad (\text{A13})$$

where $\rho_{\text{ej}}(r)$ is the density profile of the SNR. After the collision with the reverse shock, if the PWN is moving faster than its surroundings we determine the mass of the ejecta shell recently swept up by the PWN and add it to the value of $M_{\text{sw,pwn}}$ calculated at the time of the reverse shock collision. If the PWN is moving slower than its surroundings, we assume that $M_{\text{sw,pwn}}$ remains constant, even if the PWN is being compressed by the surrounding SNR. Due to the difference in pressure between the PWN interior to the mass shell and the SNR exterior to the mass shell ($P_{\text{snr}}(r = R_{\text{pwn}})$), the mass shell is subject to a force $F_{\Delta P}$, defined as:

$$F_{\Delta P} = 4\pi R_{\text{pwn}}^2 [P_{\text{pwn}} - P_{\text{snr}}(R_{\text{pwn}})]. \quad (\text{A14})$$

In this notation, $F_{\Delta P} > 0$ means that the PWN interior has a higher pressure than inside the surrounding SNR. If the PWN has not yet encountered the RS, we assume that $P_{\text{snr}}(r = R_{\text{pwn}}) = 0$. If the mass shell is moving faster than the sound speed of the surrounding material ($v_{\text{pwn}} > c_s(R_{\text{pwn}})$), which is the case before the PWN interacts with the RS (Chevalier & Fransson 1992), the mass shell is decelerated by ram pressure, and the total force on the mass swept-up by the PWN, F_{pwn} , is:

$$F_{\text{pwn}} = F_{\Delta P} - 4\pi R_{\text{pwn}}^2 \rho_{\text{ej}}(R_{\text{pwn}}) [v_{\text{pwn}} - v_{\text{ej}}(R_{\text{pwn}})]^2. \quad (\text{A15})$$

If $v_{\text{pwn}} < c_s$, then $F_{\text{pwn}} = F_{\Delta P}$. For $t \ll \tau_0$, analytical solutions to these equations give $R_{\text{pwn}} \propto t^{6/5}$ if the PWN is still inside the central constant-density core – a result which is reproduced by our numerical implementation of the model described in §4.

In this framework, the period P of a neutron star evolves as:

$$P = P_0 \left(1 + \frac{t}{\tau_0} \right)^{\frac{p-1}{p+1}}, \quad (\text{A16})$$

the period-derivative \dot{P} evolves as:

$$\dot{P} = \frac{P_0}{2\tau_0} \left(1 + \frac{t}{\tau_0} \right)^{-\frac{p-1}{p+1}} \quad (\text{A17})$$

and the surface magnetic field B_{ns} of the neutron star, assuming $p = 3$, is:

$$B_{\text{ns}} = 1.5 \left(\frac{E_{0,37}^{\frac{1}{2}} P_{0,\text{ms}}^2}{R_{14}^3} \right) \times 10^9 \text{ G} \quad (\text{A18})$$

where $E_{0,37} = \dot{E}_0/10^{37} \text{ ergs s}^{-1}$, $P_{0,\text{ms}}$ is the initial period in ms, and R_{14} is the radius of the neutron star $R/14 \text{ km}$. Additionally, for $p = 3$ τ_0 is equal to:

$$\tau_0 = 17.3 \frac{I_{45} P_{0,\text{ms}}^2}{B_{12}^2 R_{14}^6} \text{ years} \quad (\text{A19})$$

where $I = 10^{45} I_{45} \text{ g cm}^2$ and the angle between the spin and magnetic field axes of the neutron star is $\alpha = 45^\circ$.